

1 **Drainage area, bedrock fracture spacing, and weathering controls on landscape-scale**  
2 **patterns in surface sediment grain size**

3  
4 **Alexander. B. Neely<sup>1</sup> and Roman. A. DiBiase<sup>1,2</sup>**

5 <sup>1</sup>Department of Geosciences, Pennsylvania State University, University Park, Pennsylvania,  
6 USA 16802

7 <sup>2</sup>Earth and Environmental Systems Institute, Pennsylvania State University, University Park,  
8 Pennsylvania, USA 16802

9  
10 Corresponding author: Alexander B. Neely ([abn5031@psu.edu](mailto:abn5031@psu.edu))

11 **Key Points:**

- 12 • Surface sediment grain size coarsens ~10-fold downstream in steep, headwater colluvial  
13 channels and fines downstream in fluvial channels.
- 14 • Surface sediment grain size is tightly coupled to bedrock fracture spacing in steep, rocky  
15 catchments.
- 16 • Grain size is sensitive to erosion rate in soil-mantled landscapes, but invariant once  
17 bedrock hillslopes emerge.  
18

**19 Abstract**

20 Sediment grain size affects river function at the reach and landscape scale; yet, models of grain  
21 size delivery to river networks remain unconstrained due to a scarcity of field data. We analyze  
22 how bedrock fracture spacing and hillslope weathering influence landscape-scale patterns in  
23 surface sediment grain size across gradients of erosion rate and hillslope bedrock exposure in the  
24 San Gabriel Mountains (SGM) and northern San Jacinto Mountains (NSJM) of California, USA.  
25 Using ground-based structure-from-motion photogrammetry models of 50 bedrock cliffs, we  
26 quantified bedrock fracture spacing and show that fracture density is  $\sim 5\times$  higher in the SGM  
27 than the NSJM. 274 point count surveys of surface sediment grain size measured in the field and  
28 from imagery show a strong drainage area control on sediment grain size, with systematic  
29 downstream coarsening on hillslopes and in headwater colluvial channels transitioning to  
30 downstream fining in fluvial channels. In contrast to prior work and predictions from a simple  
31 hillslope weathering model, sediment grain size does not increase smoothly with increasing  
32 erosion rate. For soil-mantled landscapes, sediment grain size increases with increasing erosion  
33 rates; however, once bare bedrock emerges on hillslopes, sediment grain size in both the NSJM  
34 and SGM becomes insensitive to further increases in erosion rate and hillslope bedrock exposure,  
35 and instead reflects fracture spacing contrasts between the NSJM and SGM. We interpret this  
36 threshold behavior to emerge in steep landscapes due to efficient delivery of coarse sediment  
37 from bedrock hillslopes to channels and the relative immobility of coarse sediment in steep  
38 fluvial channels.

**39 Plain language Summary**

40 Sediment is produced from fractured bedrock on hillslopes and delivered to rivers. The size of  
41 sediment in rivers controls the size of floods or the morphology of river channels needed to move  
42 sediment downstream. It is unclear how sediment grain size delivered to river channels changes  
43 when (1) bedrock has a different fracture spacing or (2) when erosion rates control the extent of  
44 sediment grain size reduction from weathering on hillslopes. We isolate two landscapes with  
45 different bedrock fracture spacing and compare bedrock fracture spacing measured on bedrock  
46 cliffs to the size of sediment in river channels. Also, within these two landscapes, we compare  
47 sediment grain size to bedrock fracture spacing in watersheds where erosion rates are rapid and  
48 where erosion rates are slow to analyze how time-dependent weathering processes reduce the  
49 size of sediment on hillslopes. We find that when erosion rates are low, sediment weathers on  
50 hillslopes, and the grain size of river sediment is finer than bedrock fracture spacing in both  
51 landscapes. When erosion rates are higher, sediment is removed from hillslopes relatively  
52 quickly, so the grain size of river sediment reflects the initial grain size of the sediment set by  
53 bedrock fracture spacing.

54

## 55 Introduction

56 Hillslope sediment input is an important boundary condition to river function. On the  
57 timescale of individual storms, the size distribution of material delivered to river networks  
58 influences the magnitude and style of sediment transport by floods and debris flows (Parker,  
59 1990; Rickenmann, 2001; Prancevic et al., 2014). Over geologic timescales, river morphology  
60 adjusts to hillslope sediment inputs (Sklar & Dietrich, 2006; Phillips & Jerolmack, 2016), and  
61 sediment grain size can influence stream longitudinal profiles and landscape relief, complicating  
62 interpretations of climate and tectonics from topography (Hack, 1957; Kirby & Whipple, 2012).  
63 In depositional settings, changes in the down-fan extent of coarse gravel deposits are often  
64 interpreted as temporal changes in climate or tectonics, but similar depositional patterns can also  
65 result from changes in hillslope grain size inputs from river headwaters (Duller et al., 2010).  
66 Despite its importance, few field data are available to constrain the controls on network-scale  
67 sediment grain size in mountain landscapes.

68 Predicting the size of sediment delivered to river channels remains a challenging  
69 problem. Clasts are produced from fresh bedrock cut by connecting fracture planes, which sets  
70 initial sediment grain size (Palmstrom, 2005). As clasts are exhumed, they pass through the near-  
71 surface weathering zone on hillslopes where grain size reduction is accomplished by mineral  
72 dissolution (e.g., Fletcher & Brantley, 2010) and the generation of new connecting fractures  
73 through a variety of processes that may vary depending on climate, biota, mineralogy, and  
74 topography (e.g., Riebe et al., 2017). Thus, at the scale of individual hillslopes, the size of  
75 sediment delivered to rivers is expected to depend on the initial properties of the inherited  
76 bedrock fracture network, the residence time of clasts in the weathering zone, and the rate of  
77 chemical and physical weathering processes (Sklar et al., 2017). Expanding this framework to  
78 the watershed scale and comparing theory to field data requires an additional understanding of  
79 sorting and abrasion that both occur as sediment is transported through the sediment routing  
80 network (e.g., Benda & Dunne, 1997a; 1997b; Brummer & Montgomery, 2003; Attal & Lavé,  
81 2006).

82 Few studies assimilate data that can be used to test controls on landscape-scale patterns in  
83 sediment grain size outlined in the above conceptual framework. Detailed measurements of  
84 hillslope and channel sediment grain size in the northern California (Attal et al., 2015) and  
85 southern Italy (Roda-Boluda et al., 2018) showed that the size of sediment in rivers coarsens as  
86 hillslopes steepen, catchment erosion rates increase, and sediment residence time in the  
87 weathering zone decreases. Results from these studies inform conceptual models that couple  
88 river incision rates and hillslope sediment grain size inputs (Scherler et al., 2017; Shobe et al.,  
89 2018). However, these studies do not directly account for: (1) the initial size of clasts set by  
90 bedrock fracture spacing; (2) the transition from soil-mantled to bare-bedrock hillslopes; or (3)  
91 downstream sorting trends that can complicate comparisons of grain size between different  
92 channel-network positions.

93 Extending analysis of hillslope sediment grain size to steep, rocky landscapes is needed  
94 to examine the connection between bedrock fracture spacing and hillslope sediment inputs. By  
95 measuring bedrock fracture spacing on bare-bedrock hillslopes, the initial clast size can be more  
96 robustly quantified in steep, rocky landscapes than in soil-mantled landscapes (e.g. Moore et al.,  
97 2009; Messenzehl et al., 2018). Moreover, rocky hillslopes are characteristic of many steep  
98 landscapes (DiBiase et al., 2012; Milodowski et al., 2015), and the grain size of sediment  
99 supplied from steep rocky hillslopes is a key end-member when describing the range of possible

100 sediment grain sizes supplied to downstream river channels during the lifespan of a mountain  
101 range.

102 In this study, we isolate the San Gabriel Mountains and northern San Jacinto Mountains  
103 in southern California, where a contrast in bedrock fracture spacing is prevalent on bare-bedrock  
104 hillslopes, and sediment residence time in the weathering zone systematically changes as  
105 catchment erosion rates increase by 2–3 orders of magnitude in concert with steepening  
106 hillslopes and increasing bare-bedrock hillslope abundance (DiBiase et al., 2010; DiBiase et al.,  
107 2012; Heimsath et al., 2012; Neely et al., 2019). We use ground-based structure-from-motion  
108 photogrammetry to create scaled and georeferenced orthophotos of bedrock cliffs, which enable  
109 mapping of the bedrock fracture network and quantification of proxies for initial clast size  
110 distributions. We then compare initial clast size distributions from bedrock cliffs to  
111 measurements of surface sediment grain size taken from hillslopes and throughout channel  
112 networks to quantify systematic grain size sorting patterns at the landscape scale. To analyze  
113 weathering controls on sediment grain size, we compare our measurements and published  
114 erosion rates to a grain size fining model that depends on bedrock fracture spacing and sediment  
115 residence time in the weathering zone. Then, we discuss the role of selective transport and  
116 deposition on network-scale patterns in grain size and the implications for interpreting the  
117 topography of steep landscapes.

## 118 **2. Study Area/Prior work**

119 We compared bedrock fracture spacing, sediment grain size, and erosion rate throughout  
120 watersheds in the San Gabriel Mountains (SGM) and northern San Jacinto Mountains (NSJM) in  
121 southern California, USA (Fig. 1). Both landscapes have broadly similar lithology, climate, and  
122 vegetation, and each landscape has a robust inventory of detrital in-situ  $^{10}\text{Be}$  data that show a  
123 spatial pattern in catchment erosion rate that correlates with changes in mean hillslope angle and  
124 bare-bedrock exposure on hillslopes (DiBiase et al., 2010; DiBiase et al., 2012; Heimsath et al.,  
125 2012; Neely et al., 2019). Erosion rates in the SGM range from 0.036–2.2 m kyr<sup>-1</sup> (DiBiase et al.,  
126 2010; DiBiase et al., 2012; Heimsath et al., 2012; Neely et al., 2019) and erosion rates in the  
127 NSJM span from 0.04–0.61 m kyr<sup>-1</sup> (Rossi, 2014; Neely et al., 2019). Hillslopes in both the SGM  
128 and NSJM range from fully soil-mantled to ~70% bare-bedrock at the scale of headwater (<7  
129 km<sup>2</sup>) catchments, and field observations and soil pits indicate similar soil thicknesses (<1 m) on  
130 soil-mantled hillslopes throughout both landscapes (DiBiase et al., 2012; Heimsath et al., 2012;  
131 Neely et al., 2019). There is no evidence of Plio-Pleistocene glaciation in either landscape.

132 The primary difference between the San Gabriel Mountains and northern San Jacinto  
133 Mountains is a contrast in bedrock fracture density driven by differences in tectonic setting,  
134 which leads to a contrast in initial hillslope grain size inputs between the two landscapes (Fig. 2).  
135 DiBiase et al. (2018) used scaled field photographs to measure an approximate 5× contrast in  
136 fracture spacing between a single cliff from each landscape, with higher bedrock fracture density  
137 in the SGM. In this study, we build on these measurements by quantifying bedrock fracture  
138 spacing from structure-from-motion photogrammetry models of 50 bedrock cliffs distributed  
139 throughout headwater catchments in the NSJM and SGM.

140 In both landscapes, hillslopes remain relatively soil-mantled until mean hillslope angles  
141 exceed approximately 35°, consistent with a threshold hillslope stability angle for soil-mantled  
142 hillslopes (Carson & Petley, 1970). This hillslope morphology corresponds to erosion rates of  
143 0.08 m kyr<sup>-1</sup> in the NSJM and 0.2 m kyr<sup>-1</sup> in the SGM, reflecting more efficient soil production

144 from fractured bedrock in the SGM (Neely et al., 2019). Above mean hillslope angles of 35°,  
145 exposure of bare-bedrock hillslopes increases with increasing mean hillslope angle in both  
146 landscapes (DiBiase et al., 2012; Neely et al., 2019).

147 Steep hillslopes in the SGM and NSJM are connected to fluvial channels by constant-  
148 gradient colluvial channels typically mantled in sediment perched near the angle of repose (33°–  
149 35°) and thought to be primarily transported by mass wasting and debris flow processes (Stock  
150 and Dietrich, 2006; DiBiase et al., 2018). The morphologic transition from constant-slope  
151 headwater channels to fluvial channels with characteristic concave-up longitudinal profiles  
152 (Montgomery & Foufoula-Georgiou, 1993) occurs at drainage areas of 0.08–0.8 km<sup>2</sup> in the SGM  
153 and 0.5–2 km<sup>2</sup> in the NSJM (DiBiase et al., 2012; DiBiase et al., 2018). Headwater colluvial  
154 channels have similar gradients between both landscapes, while fluvial channels are steeper in  
155 the NSJM than the SGM despite having lower catchment averaged erosion rates. The contrast in  
156 fluvial steepness was attributed to coarser sediment grain size and wider channels measured in  
157 fans of catchments the NSJM than in fans of catchments in the SGM (DiBiase et al., 2018).

158 We build on existing sediment grain size data in the NSJM and SGM by systematically  
159 measuring stream grain size from fractured bedrock to depositional fans, and we target  
160 catchments that span the full range of erosion rates measured in both landscapes. Existing  
161 sediment grain size analyses in the NSJM and SGM (DiBiase et al., 2011; DiBiase et al., 2018)  
162 do not consider systematic changes in sediment grain size as a function of position in the  
163 sediment routing network (e.g. Brummer & Montgomery, 2003; Attal & Lavé, 2006).  
164 Additionally, surveys were taken primarily in catchments with steep hillslopes, and do not span  
165 the full range of catchment averaged erosion rates observed in both landscapes (DiBiase et al.,  
166 2011; DiBiase et al., 2018).

### 167 **3. Methods**

#### 168 *3.1 Fracture mapping of exposed bedrock cliffs*

169 To constrain initial clast size distributions for each landscape, we measured bedrock  
170 fracture density on 50 cliffs in the NSJM (n = 21) and SGM (n = 29) using cliff-normal  
171 orthophotos extracted from scaled and georeferenced structure-from-motion photogrammetry  
172 models of cliff faces ranging in size from 10<sup>2</sup>–10<sup>5</sup> m<sup>2</sup> (Fig. 3). Photos were taken from ridgeline  
173 camera stations opposite cliffs at distances of 50–1500 m with a Nikon D5500 digital single-lens  
174 reflex camera using telephoto lenses (55 and 300 mm focal lengths). The location for each  
175 camera station was determined using an EOS Arrow 100 Bluetooth Global Navigation Satellite  
176 System (GNSS) receiver (uncertainties typically <5 m). We used Agisoft PhotoScan v1.4.0  
177 (<https://www.agisoft.com/>) to align GNSS-tagged photographs and construct dense point clouds  
178 with an average point spacing of 0.1–1 cm. We refined the alignment of each dense point cloud  
179 through iterative closest point alignment to georeferenced airborne lidar point clouds (average  
180 point spacing of 10–100 cm) using the software CloudCompare  
181 (<https://www.cloudcompare.org/>) (e.g. Neely et al., 2019). We used the aligned and  
182 georeferenced dense point clouds to generate a three-dimensional mesh and then constructed  
183 orthophotos from a view perpendicular to the target cliff face, with orthophoto resolutions of 1–3  
184 cm (see supplementary dataset).

185 Bedrock fractures were traced as line features on scaled orthophotos in ESRI ArcMAP  
186 v10.6.1 to derive two measures of bedrock fracturing (Fig. 3B). First, we calculated bedrock

187 fracture density ( $\text{m m}^{-2}$ ) as a ratio of the total length of bedrock fracture traces and the area over  
188 which bedrock fractures were traced (Dershowitz & Herda, 1992). Second, as a proxy for the  
189 initial size distribution of clasts delivered from cliffs, we measured the bedrock fracture spacing,  
190 which we define as the apparent short-axis length for each fracture-bound area lying at the  
191 intersection of a 2 m grid overlain on the orthophoto (Bunte & Abt, 2001). We assumed that the  
192 initial grain size distribution of hillslope clasts in fresh bedrock is set by the bedrock fracture  
193 spacing distribution, which may underestimate the intermediate axis of clasts if the short axis is  
194 exposed on the cliff face or the orthophoto plane is oriented skew to regional joint sets. To  
195 minimize this error, we extracted orthophotos primarily on planar cliff faces perpendicular to  
196 joint sets. In contrast, bedrock fracture spacing may overestimate the initial grain size of  
197 sediment if clast detachment occurs along finer-scale discontinuities, such as mineral-grain  
198 boundaries.

### 199 *3.2 Sediment grain size distributions on hillslopes and in channels*

200 We used a combination of field point counts, field-based structure-from-motion  
201 photogrammetry models of deposits, and aerial orthophoto surveys to measure surface grain size  
202 distributions on hillslopes and throughout channel networks in the SGM and NSJM (Fig. 1). A  
203 variety of survey types were required to measure sediment grain size due to accessibility  
204 restrictions and the difficulty of measuring coarse ( $>1$  m diameter) grains using tape-measure-  
205 based point counts. The resulting 274 grain size surveys have sample sizes of 40–700 individual  
206 grains and sample a wide range of hillslope and channel positions (drainage area ranges from  
207  $10^2$ – $10^7$   $\text{m}^2$ ).

208 For field point counts, a 50 m tape measure was laid across the survey reach in 2–6  
209 longitudinal sections spaced 1 m apart in the SGM and 2 m apart in the NSJM, and we measured  
210 the intermediate axis of each grain intersected by a meter mark (Wolman, 1954). Field surveys  
211 were conducted in summers of 2016, 2017, 2018, and 2019. Surface sediment grain size was  
212 measured to millimeter precision in sand and pebble-dominated reaches and centimeter precision  
213 in cobble and boulder-dominated reaches.

214 For field-based structure-from-motion photogrammetry surveys, we photographed  
215 deposits from multiple vantage points using either a Nikon D5500 digital single-lens reflex  
216 camera with a wide-angle lens (12 mm focal length), an Apple iPhone 4s, or an Apple iPhone 5s.  
217 All cameras produced models with point spacing at the millimeter scale because photographs  
218 were taken at relatively close range ( $<10$  m). We used Agisoft PhotoScan v1.4.0 to align  
219 photographs and generate dense point clouds. Along the edges of each survey region, we  
220 included 1–6 scale bars which were used to scale the model and check for distortion, which is  
221 typically  $<2\%$ . For each survey, we generated a high-resolution three-dimensional mesh and 0.1-  
222 1 cm resolution orthophoto from a view perpendicular to the deposit surface. Scaled orthophotos  
223 were loaded into ArcMAP 10.6.1 and overlain by a grid with a spacing typically larger than half  
224 the width of the largest grain. We measured the apparent short axis of each grain overlain by a  
225 grid intersection point using the grid-by-number method (Bunte and Abt, 2001). Large boulders  
226 that span multiple intersection points were counted at each grid intersection and for 3 surveys in  
227 the SGM, the largest boulders ( $> 15$  m diameter) comprise as much as  $\sim 20\%$  of individual survey  
228 areas, leading to large  $D_{84}$  values in these individual surveys.

229 In locations with coarser sediment cover, grain size measurements were made  
230 continuously on 6–17 cm resolution georeferenced orthophotos from commercial imagery

231 spanning 2011–2017 (Pictometry Corp.; <https://www.eagleview.com/product/pictometry->  
232 [imagery/](https://www.eagleview.com/product/pictometry-imagery/)) (Fig. 4). Similar to the structure-from-motion photogrammetry surveys, we used the  
233 grid-by-number method (Bunte & Abt, 2001) to measure the apparent short-axis dimension in  
234 planview (assumed to correspond to the intermediate axis) of all clasts in the active channel that  
235 intersected a 2 m grid. The minimum resolved grain diameter was set to 4 pixels and grid  
236 intersections obscured by vegetation or water were not included in the grain size distribution. We  
237 defined grain size measurements below the resolving limit (24–68 cm) as “fine” and included  
238 these values in the construction of cumulative grain size distributions (e.g. DiBiase et al., 2018).  
239 To calculate grain size distributions and facilitate comparison with field-derived data, the  
240 continuous channel surveys were broken up into 50 - 200 m long reaches consisting of 70–400  
241 grains each, depending on tributary junctions and changes in channel width.

242 To quantify uncertainty in our measurements of median grain size,  $D_{50}$ , we performed a  
243 bootstrap analysis that considers the full range of measured grain sizes within each landscape  
244 (0.1–1594 cm). We recorded the  $D_{50}$  from distributions that contained 1–1000 grains randomly  
245 subsampled from full distributions containing 1706 grains in the NSJM and 3981 grains in the  
246 SGM. At the 95% confidence interval,  $D_{50}$  from subsampled distributions containing 100  
247 individual grains varied by ~30% relative to the  $D_{50}$  of the full distribution. This variability  
248 reduced to ~15% for subsample sizes containing 500 individual grains, which is typical for  
249 amalgamated grain size surveys that consider all surveys taken near  $^{10}\text{Be}$  samples, and are used  
250 to fit model calculations outline in sections below (Table 1).

### 251 *3.3 Catchment-averaging of fracture density and grain size data*

252 Our analysis focuses on catchments with published catchment averaged erosion rates and  
253 bedrock hillslope abundance, and within these catchments, we measured bed sediment grain size  
254 and constrain bedrock fracture spacing on representative cliffs. Published catchment averaged  
255 erosion rates were tied to catchment outlets of larger catchments (drainage area  $>7 \text{ km}^2$ ) and  
256 smaller, headwater catchments (drainage areas  $0.6\text{--}7 \text{ km}^2$ ). At each  $^{10}\text{Be}$  sample location, we  
257 compiled nearby fan grain size surveys (drainage area  $>7 \text{ km}^2$ ) or fluvial channel head grain size  
258 surveys (drainage areas  $0.05\text{--}3 \text{ km}^2$  and  $0.5\text{--}7 \text{ km}^2$  in the SGM and NSJM respectively). For  
259 larger catchments (drainage area  $>7 \text{ km}^2$ ), we estimated bedrock hillslope abundance using linear  
260 regressions between mean hillslope angle and bedrock hillslope abundance in the NSJM and  
261 SGM (Neely et al., 2019) (Table 1).

262 In all comparisons between sediment grain size and catchment averaged erosion rate, we  
263 assume that bed sediment grain size reflects an average bed-state condition over timescales  
264 integrated by  $^{10}\text{Be}$ -derived erosion rates ( $10^2\text{--}10^6$  years). While significant surface grain size  
265 variability might be expected at the reach scale over these timescales (e.g. Benda and Dunne,  
266 1997b), our analysis compiles 274 individual grain size surveys over regions of  $>100 \text{ km}^2$  (Fig.  
267 1), and it is unlikely that grain size surveys spanning the spatial scale of our analysis reflect a  
268 single, recent large-magnitude event that affected both the NSJM and SGM. In particular, we  
269 avoided sampling areas that had been burned within the previous 5 years to avoid bias by fine-  
270 grained dry sediment loading (e.g., Lamb et al., 2011).

271 Within each catchment, bedrock fracture density and bedrock fracture spacing  
272 measurements were estimated from sample sizes ranging from 0 to 14 cliffs (Table 1). Our  
273 ability to resolve local differences in bedrock fracture spacing between watersheds within each  
274 landscape is limited; however, the 21–29 cliffs with bedrock fracture measurements in the NSJM

275 and SGM characterize the range of grain size inputs at the scale of each landscape (Fig. 3). We  
 276 used the summed distribution of all bedrock fracture spacing measurements within each  
 277 landscape (NSJM or SGM) to determine the grain size inputs to each catchment, and we assumed  
 278 that changes in bedrock fracture spacing between catchments within each landscape are small  
 279 compared to larger contrasts in bedrock fracture spacing between the NSJM and SGM (Table 1).

### 280 3.4 Hillslope sediment grain size fining model

281 We compared our measurements of sediment grain size from fluvial channel heads to that  
 282 predicted from a model of hillslope sediment supply that accounts for changes in bedrock  
 283 fracture spacing and a time-dependent grain size reduction due to the residence time of clasts  
 284 within the near surface weathering zone. We used field data from fluvial channel heads as a  
 285 comparison to the model to minimize the effect of systematic downstream grain size sorting,  
 286 which is not accounted for. Additionally, sediment is coarsest at the fluvial channel head and  
 287 thus provides a minimum bound on the degree of grain size reduction due to weathering.

288 We modified a simple model of hillslope grain size reduction used for soil-mantled  
 289 landscapes (Sklar et al., 2017) to account for the observed transition to bare-bedrock hillslopes  
 290 that occurs as landscapes steepen and erosion rates increase (DiBiase et al., 2012; Neely et al.,  
 291 2019). The median grain size of sediment delivered to channels from hillslopes,  $D_{50\ channel}$ , is  
 292 modeled according to:

$$293 \quad D_{50\ channel} = (1 - f_{bedrock}) (k_1 D_{50\ fracture} - k_2 t) + f_{bedrock} k_3 D_{50\ fracture} \quad (1)$$

294 where  $f_{bedrock}$  is the fraction of bare bedrock in the catchment,  $D_{50\ fracture}$  is the  $D_{50}$  of bedrock  
 295 fracture spacing measurements,  $t$  is the time spent in the weathering zone, and  $k_1$ ,  $k_2$ , and  $k_3$  are  
 296 fining constants. Based on field data,  $f_{bedrock}$  can be described by:

$$297 \quad f_{bedrock} = \alpha(E - E_{crit}) \quad (2)$$

298 where  $E$  is the catchment averaged erosion rate,  $E_{crit}$  is erosion rate at which significant bedrock  
 299 exposure occurs, and  $\alpha$  describes how the abundance of bare-bedrock hillslopes increases with  
 300 increasing erosion rate (Neely et al., 2019). The value of  $f_{bedrock}$  is limited to a maximum of 1,  
 301 which reflects a condition where all hillslopes within a catchment are bare-bedrock hillslopes.  
 302 The residence time in the weathering zone,  $t$ , is defined by:

$$303 \quad t = h/E \quad (3)$$

304 where  $h$  is thickness of weathering zone (e.g. Attal et al., 2015).

305 The constants  $k_1$  and  $k_3$  determine the immediate grain size reduction due to breakage in  
 306 rockfall or clast detachment along fractures that are below the resolving limit of our fracture  
 307 spacing measurements (Fig. 5). Because of challenges in measuring initial clast size on soil-  
 308 mantled hillslopes, we assume this mechanism is the same under soil as on bedrock cliffs ( $k_1 =$   
 309  $k_3$ ).  $k_2$  is a rate constant that defines time-dependent mechanisms of grain size reduction (Fig. 5).  
 310 More specific parameterizations that describe sediment fining on hillslopes as a function of  
 311 additional environmental variables could be substituted for  $k_2$  (e.g. Sklar et al., (2017); Riebe et  
 312 al., (2017)); however, bedrock fracture spacing appears to be the primary control on the contrast  
 313 in hillslope erosion and morphology across the SGM and NSJM (Neely et al., 2019), and we  
 314 assume a constant fining rate in the absence of more specific field constraints.

315 Equation 1 reflects a linear mixing model between sediment supplied from soil-mantled  
 316 and bare-bedrock hillslopes, and thus additional constraints are needed to describe the  
 317 morphodynamics of patchy soil and bedrock hillslopes. For simplicity, we assume that soil-  
 318 mantled and bare-bedrock hillslopes are eroding at the same rate in the SGM and NSJM (Neely  
 319 et al., 2019). We also assume that  $D_{50\text{ fracture}}$  is the fracture spacing measured on bedrock cliffs,  
 320 and additional weathering of clasts during transit to channels is accounted for by the value of  $k_3$ .  
 321 For soil mantled hillslopes, we assume for simplicity that the average weathering zone thickness,  
 322  $h$ , is uniform (Heimsath et al., 2012) and thus the residence time of sediment in the weathering  
 323 zone of soil-mantled hillslopes depends only on erosion rate.

324 To compare the model results to field data, we assumed that  $D_{50\text{ channel}}$  corresponds to the  
 325 median grain size of fluvial channel head grain size surveys from headwater catchments where  
 326 the erosion rate,  $E$ , is determined from  $^{10}\text{Be}$  concentrations in stream sediments. Although we  
 327 focus on the evolution of  $D_{50}$ , similar results would arise from using, for example, the 84<sup>th</sup>  
 328 percentile grain size ( $D_{84}$ ) due to limited variation in sorting across surveys from the SGM and  
 329 NSJM (Fig. 6). The values of  $E_{crit}$  and  $D_{50\text{ fracture}}$  for each catchment should depend primarily on  
 330 rock properties. We assume values of  $E_{crit}$  previously calculated for the NSJM and SGM (Neely  
 331 et al., 2019) and use landscape-averaged values for  $D_{50\text{ fracture}}$  in each landscape determined from  
 332 fracture spacing measurements on 50 cliff-normal orthophotos.

333 To determine grain size fining constants, we calibrate the initial fining coefficient,  $k_1=k_3$ ,  
 334 and fining rate coefficient,  $k_2$ , using a brute-force iteration through a range of parameter values.  
 335 Equation 1 asymptotes at two positions: (1) when sediment residence time in the weathering  
 336 zone is long and sediment is fined to a minimum grain size and (2) at the product of  $D_{50\text{ fracture}}$   
 337 and  $k_3$ , the maximum possible modeled grain size (assuming  $k_1=k_3$ ). A minimum grain size value  
 338 of 0.01 cm was chosen, because this value is significantly finer than all field measurements, and  
 339 model fits are not affected by the choice of this boundary condition. Because residuals between  
 340 model fits and field data exceeding these criteria are infinite, we calculate residuals in both the  
 341 non-dimensional median grain size,  $D_{50}$ , ( $y$ ) and non-dimensional erosion rate,  $E$ , ( $x$ ) directions  
 342 (Fig. 5). We use the minimum of these two residuals for each field data point to calculate least-  
 343 squared summed residual, which defined the best-fit  $k_3$  and  $k_2$  parameter combination for each  
 344 landscape.

## 345 4. Results

### 346 4.1 Bedrock fracture density and bedrock fracture spacing distributions

347 The mean fracture density of 29 bedrock cliffs in the SGM is  $1.8 \pm 0.4$  (1 SD)  $\text{m m}^{-2}$ , and  
 348 the mean fracture density of 20 bedrock cliffs in the NSJM is  $0.46 \pm 0.12$   $\text{m m}^{-2}$ . Across SGM  
 349 cliffs, bedrock fracture density ranges from 0.56–4.7  $\text{m m}^{-2}$ , whereas bedrock fracture density  
 350 varies over a smaller range, 0.34–1.2  $\text{m m}^{-2}$ , across cliffs in the NSJM (Fig. 3, 7). Combining all  
 351 bedrock cliffs surveyed, the median bedrock fracture spacing,  $D_{50\text{ fracture}}$ , is 63 cm in the SGM  
 352 (3112 measurements) and 299 cm in the NSJM (2344 measurements). For individual cliffs  
 353 within each landscape,  $D_{50\text{ fracture}}$  ranges from 34–339 cm in the SGM and from 93–482 cm in the  
 354 NSJM (Fig. 7). As expected, there is an inverse relationship between the fracture density and  $D_{50}$   
 355 *fracture* across all cliffs (Fig. 7). The 4-5-fold contrast in both bedrock fracture density and bedrock  
 356 fracture spacing between the NSJM and SGM consistently suggests a 4-5-fold contrast in initial

357 sediment grain size inputs between both landscapes and is in qualitative agreement with regional  
358 observations (DiBiase et al., 2018).

#### 359 *4.2 Surface sediment grain size distributions on hillslopes and in channels*

360 Within both landscapes, sediment grain size varies by ~2-3 orders of magnitude  
361 depending on the catchment erosion rate, drainage area, and the grain size distribution statistic  
362 analyzed (i.e.,  $D_{16}$ ,  $D_{50}$ ,  $D_{84}$ ); however, when isolating these variables, sediment grain size is  
363 consistently coarser in NSJM than the SGM (Fig. 8). The  $D_{50}$  of all grain size measurements is  
364 55 cm in the NSJM and 17 cm in the SGM, and the  $D_{84}$  of all grain size measurements is 184 cm  
365 in the NSJM and 67 cm in the SGM.

366 In both landscapes, sediment grain size varies by 1-2 orders of magnitude through  
367 systematic downstream sorting trends. Sediment grain size coarsens with increasing drainage  
368 area along headwater colluvial channels until reaching fluvial channel heads, where downstream  
369 coarsening transitions to downstream fining throughout the fluvial channel network (Fig. 8). The  
370 transition from downstream coarsening to downstream fining corresponds to a morphologic  
371 transition from steep, constant-gradient colluvial channels to concave fluvial channels at  
372 drainage areas between 0.08 km<sup>2</sup> and 0.8 km<sup>2</sup> in the SGM and 0.5 and 2 km<sup>2</sup> in the NSJM (Fig.  
373 8; DiBiase et al., 2018).

#### 374 *4.3 Erosion rate controls on sediment grain size*

375 Between gentle soil-mantled catchments and steep catchments with abundant bedrock  
376 hillslopes, there is a contrast in the dependency between catchment erosion rate and stream grain  
377 size. When catchments are mostly soil-mantled, stream grain size distributions are similar in the  
378 SGM and NSJM but coarsen as erosion rates increase in both landscapes, with  $D_{50}$  ranging from  
379 0.5–6 cm (Fig. 9). In steep, rocky catchments, where  $E > E_{crit}$ , sediment grain size remains  
380 relatively constant despite increasing catchment erosion rates;  $D_{50}$  at fluvial channel heads is 90–  
381 150 cm in the NSJM and 20-40 cm in the SGM, and  $D_{50}$  at fans is 29–60 cm in the NSJM and 8–  
382 22 cm in the SGM.

#### 383 *4.4 Comparison of field data with predictions from hillslope sediment fining model*

384 In both the NSJM and SGM, the coarsest sediment grain size distributions at fluvial  
385 channel heads are approximately half the input grain size distributions estimated from bedrock  
386 fracture spacing ( $D_{50\text{ fracture}}$ ), requiring an immediate grain size reduction coefficient,  $k_1 = k_3$ , of  
387 0.4–0.5 (Fig. 10). Best-fit fining rates ( $k_2$ ) are 0.05 m kyr<sup>-1</sup> and 0.025 m kyr<sup>-1</sup> in the NSJM and  
388 SGM respectively, which suggests that despite similar bedrock mineralogy and climate, sediment  
389 grain size reduction is ~2× faster on hillslopes in the NSJM than the SGM. When erosion rates  
390 are rapid and bare-bedrock hillslopes are abundant, changes in catchment-averaged hillslope  
391 sediment residence time are small (~ 100–1000 years) relative to best-fit fining rates ( $k_2$ ), and  
392 modeled hillslope sediment grain sizes supplied to channels are relatively invariant across a wide  
393 range of relatively rapid catchment erosion rates ( $E > E_{crit}$ ). However, given these best-fit fining  
394 rates ( $k_2$ ), the model does not capture the abrupt coarsening of bed sediment grain size when  
395 erosion rates near  $E_{crit}$  in both landscapes.

396 **5. Discussion**

397 Our results show three primary controls on sediment grain size measured at any particular  
398 location in a catchment: (1) downstream effects due to grain size sorting during sediment  
399 transport; (2) the initial grain size of sediment set by bedrock fracture spacing; and (3) erosion  
400 rate as a proxy for the residence time of sediment in the weathering zone. We discuss how these  
401 factors relate to processes that transport sediment through channel networks spanning a range of  
402 hillslope morphologies and erosion rates (sections 5.1-5.3), then we examine the implications of  
403 systematic grain size trends in the context of landscape evolution over geologic timescales  
404 (section 5.4).

405 *5.1 Drainage area dependent patterns in sediment grain size within each landscape*

406 In the NSJM and SGM, downslope and downstream sorting are observed at the scale of  
407 individual talus slopes and at the scale of entire watersheds, suggesting that sorting associated  
408 with sediment transport is a first order control on sediment grain size. On steep talus slopes  
409 (drainage area  $< \sim 0.01 \text{ km}^2$ ), downstream coarsening trends are consistent with results from  
410 rockfall and talus slope models and experiments (e.g., Rapp, 1960; Kirkby & Statham, 1975) and  
411 inconsistent with progressive weathering as particles move down slope, which would generate  
412 downslope fining after sediment is detached from cliffs (Glade et al., 2017). In steep catchments,  
413 sediment grain size continues to coarsen downstream throughout the headwater colluvial channel  
414 network. We hypothesize that this pattern emerges primarily as a consequence of debris flow  
415 transport of coarse-grained sediment towards the base of headwater colluvial channels, where  
416 decreases in slope often coincide with tributary junctions (Stock & Dietrich, 2006). Repeated  
417 deposition of coarse-grained debris flow snouts may concentrate coarse-grained sediment at the  
418 base of steep, headwater channels and the upstream extent of the fluvial channel network (Fig.  
419 8). The transition from downstream coarsening in headwater channels to downstream fining in  
420 fluvial channels is consistent with a transition in dominant sediment transport process at drainage  
421 areas of  $0.08\text{--}2 \text{ km}^2$  in SGM and NSJM respectively (DiBiase et al., 2012; DiBiase et al., 2018),  
422 and is broadly similar to observations of downstream coarsening in headwater channels of  
423 western Washington interpreted to be due to debris flow transport (Brummer and Montgomery,  
424 2003).

425 Fining throughout the fluvial network could be driven by selective transport, abrasion, or  
426 downstream changes in hillslope sediment grain size inputs (e.g., Pizzuto, 1995; Attal and Lavé  
427 2006; Menting et al., 2015). In both the NSJM and SGM, hillslope gradients and erosion rates do  
428 not systematically change downstream, suggesting that downstream changes in hillslope  
429 sediment grain size inputs are unlikely to drive consistent downstream fining trends. Given  
430 typical abrasion rates for granitic bedrock, abrasion is unlikely to fine sediment by 50–75% over  
431 transport distances of  $\sim 10 \text{ km}$  (Attal & Lavé, 2009). Size-selective transport is likely the primary  
432 factor that controls downstream fining trends over these small watersheds the NSJM and SGM;  
433 however, abrasion may significantly fine immobile boulders that reside in channels for long  
434 timescales relative to more mobile size clasts. The relative immobility of boulders in NSJM and  
435 SGM channels may result from large clast-sizes relative to channel width and flow depth, which  
436 promotes grain protrusion from flows and formation of reach-spanning boulder-jams. These  
437 factors preferentially increase the stability of coarse-grained sediment in steep, narrow channels  
438 with low flow depths, such that fine-grained sediment is winnowed downstream (Yager et al.,  
439 2007; Lamb et al., 2008; Zimmerman et al., 2010; Lamb et al., 2017). At larger drainage areas,

440 fluvial channels progressively widen and deepen relative to maximum clast sizes, and the relative  
441 mobility across all grain size classes may be more uniform, leading to systematic downstream  
442 fining trends.

### 443 *5.2 Bedrock fracture spacing and estimating initial sediment grain size*

444 Sediment grain size in the NSJM and SGM mirrors the  $\sim 5\times$  contrast in bedrock fracture  
445 spacing between these two landscapes, and the contrast in fracture spacing is most directly  
446 reflected in the grain size of sediment in steep, rocky catchments where sediment residence time  
447 in the weathering zone is short and sediment is effectively transported from bedrock hillslopes to  
448 channels. Yet, in steep, rocky catchments, the  $D_{50}$  of the coarsest grain size distributions are  
449 approximately half as large as the  $D_{50}$  of bedrock fracture spacing measured on cliffs ( $k_3 = 0.4$ –  
450  $0.5$ ) (Fig. 10). Contrast between estimated grain size from bedrock fracture spacing and the  
451 coarsest  $D_{50}$  grain size in channels may reflect sediment sorting, breakage during rockfall or  
452 transport, or detachment of sediment along fracture planes that have apertures below the  
453 resolution limit of our bedrock-cliff orthophotos ( $\sim 1$  cm resolution) (e.g. Messenzehl et al.,  
454 2018). More work is needed to quantify the relative importance of grain detachment along the  
455 range of fracture lengths and apertures seen in damaged rock (e.g. Barton & Zobeck et al., 1992;  
456 Hooker et al., 2014); however, a similar initial bedrock fining factor ( $k_3 = 0.4$ – $0.5$ ) determined  
457 for landscapes with a large contrast in fracture density suggests a similar grain size reduction  
458 mechanism in both landscapes and that our bedrock fracture measurements quantify a similar  
459 range of fracture geometries relevant for sediment detachment in the NSJM and SGM.

460 In contrast to steep, rocky catchments, sediment grain size in soil-mantled catchments is  
461 relatively similar between the NSJM and SGM. Similar sediment grain size but sparser bedrock  
462 fracture spacing in the NSJM than the SGM requires faster apparent grain size fining rates in the  
463 NSJM than the SGM. Bedrock mineralogy and climatic differences are minimal between these  
464 mountain ranges, and thus the drivers of faster apparent grain size fining rates in the NSJM are  
465 not immediately obvious. Potentially, more sediment on soil-mantled hillslopes is sourced from  
466 grussification along mineral-scale discontinuities rather than detachment along macrofractures.  
467 Additionally, boulders detached along fracture planes may be relatively immobile across lower-  
468 gradient hillslopes and weather as exhumed corestones during downslope transport (e.g. Fletcher  
469 & Brantley, 2010; Glade et al., 2017). Selective transport of fine-grained sediment across low-  
470 gradient hillslopes and detachment of sediment by grussification may decouple sediment grain  
471 size from bedrock fracture spacing where hillslope gradients are low, a continuous soil mantle  
472 exists, and rock is efficiently weathered.

473 The grain size distribution of sediment in talus piles has been used as a proxy for the  
474 grain size distribution of sediment contributed from bedrock cliffs (Attal et al., 2015; Roda-  
475 Boluda et al., 2018); however, in the NSJM and SGM, the grain size of sediment in talus piles is  
476 much finer (5–10 $\times$ ) than the grain size estimated from bedrock fracture spacing on cliffs (Fig. 8).  
477 On individual talus piles, clast travel distances are sensitive to talus pile slope, clast momentum  
478 following rockfall height, and the grain size of the mobile clast relative to the roughness of the  
479 talus pile surface (Kirkby & Statham, 1975; DiBiase et al., 2017). In the NSJM and SGM, the  
480 coarsest grains supplied from bedrock cliffs bypass steep talus slopes with small upstream  
481 drainage areas ( $< \sim 0.01$  km<sup>2</sup>) and are located at the base of headwater colluvial channels,  
482 meaning that the coarsest grain size fraction is not captured by the grain size distribution of  
483 sediment on individual talus slopes adjacent to source cliffs (Fig. 8). Because grain size sorting

484 occurs immediately after clasts are dislodged from intact bedrock, bedrock fracture spacing on  
485 cliffs serves as a more direct measure of the initial sediment grain size; however, more work is  
486 needed to describe controls on  $k_3$ , which describes the relationship between sediment grain size,  
487 the range of fracture lengths and apertures in a rock mass, and processes that detach clasts along  
488 fractures of different geometry (e.g. Sklar et al., 2017).

### 489 *5.3 Erosion rate and bedrock exposure controls on sediment grain size distributions*

490 In both landscapes, slowly eroding soil-mantled catchments have finer surface sediment  
491 grain size than catchments with steep, rapidly eroding threshold hillslopes with abundant bare-  
492 bedrock cliffs, indicating a residence-time dependence on stream sediment grain size. Sediment  
493 residence time in the weathering zone decreases with increasing erosion rate due to both more  
494 rapid erosion and effective thinning of the weathering zone due to increased bedrock exposure.  
495 Although the thickness of soil on soil-mantled hillslopes does not decrease considerably with  
496 increasing erosion rate in these landscapes (Heimsath et al., 2012), the abundance of bare  
497 bedrock cliffs increases (Neely et al., 2019), which thins the weathering zone at the catchment-  
498 scale.

499 The grain size of sediment at fluvial channel heads does not show smoothly coarsening  
500  $D_{50}$  grain size with decreasing sediment residence time in the weathering zone; instead, there is a  
501 dichotomy between sediment grain size in catchments with gentle, soil-mantled hillslopes and  
502 catchments with steep hillslopes and bare-bedrock cliffs (Fig. 10). A linear relationship between  
503 grain size fining and erosion rate (Eq. 1) can generally reproduce the observed stream grain sizes  
504 using fining rates ( $k_2$ ) that are consistent with typical weathering rates of bedrock tors in granitic  
505 landscapes ( $0.025\text{--}0.05\text{ m kyr}^{-1}$ ) (Portenga & Bierman, 2011); however, this model may be  
506 misleading if: (1) a different proportion of clasts are detached along fracture planes and mineral-  
507 scale discontinuities as a function of changing erosion rate and sediment residence time in the  
508 weathering zone (i.e. an erosion rate control on  $k_3$ ); or (2) if sediment is selectively transported  
509 through the river network such that grain size inputs supplied from hillslopes do not reflect the  
510 grain size of surface sediment cover at fluvial channel heads. Our channel grain size  
511 measurements indicate that erosion rates primarily control bed sediment grain size through  $E_{crit}$ ,  
512 the erosion rate at which hillslopes transition from gentle, soil-mantled morphologies to steep  
513 hillslopes with increasing abundance of bare-bedrock cliffs.

514 In contrast to the hillslope sediment fining model (Eq. 1), we interpret the sediment grain  
515 size dichotomy between gentle, soil-mantled and steep, rocky catchments to reflect a transition  
516 where bedrock exposure on steep hillslopes is a threshold that initiates delivery of coarse  
517 sediment from rockfall, landslides, and debris flows (e.g. Roda-Boluda et al., 2018). Because of  
518 the relative immobility of the coarsest grain size fraction in steep, narrow channels (e.g.  
519 Rickenmann, 2001), sediment supply from even a small amount of bedrock cliffs mantles  
520 channels with coarse sediment that directly reflects bedrock fracture spacing. Channel response  
521 to coarse sediment inputs (e.g. Shobe et al., 2016) winnows finer sediment supplied from  
522 hillslopes downstream to depositional fans, leading to observed downstream fining trends (Fig.  
523 8; Fig. 11). Although the grain size of the sediment flux exiting watersheds is likely sensitive to  
524 decreasing soil cover on hillslopes, changing the abundance of soil-mantled and bare-bedrock  
525 hillslopes as erosion rates exceed  $E_{crit}$  has minimal effect on the grain size of bed surface cover in  
526 NSJM and SGM channels (Fig. 9-11). If channel slopes are set in part by a threshold that  
527 depends on the grain size of surface cover (Lague et al., 2005; DiBiase & Whipple, 2011;

528 Phillips & Jerolmack, 2016; Pfeiffer et al, 2017), fracture density emerges as a direct control on  
529 sediment grain size and an indirect control on the steepness of rivers across a potentially wide  
530 range of hillslope erosion rates that exceed  $E_{crit}$ .

#### 531 *5.4 Implications of systematic grain size trends for landscape evolution over geologic timescales*

532 At the landscape scale, our results imply a strong connection between bedrock fracturing,  
533 sediment grain size, and the efficiency of river incision in steep mountain ranges (Molnar et al.,  
534 2007; DiBiase et al., 2018). Relative to soil-mantled hillslopes, surface sediment grain size in  
535 channels more strongly reflects contrasts in bedrock fracture spacing in steep, rocky landscapes.  
536 In steep landscapes, riverbed morphology is sensitive to coarse sediment inputs from bedrock  
537 cliffs and landslides, whereas the total flux of sediment likely includes a larger fraction of fine-  
538 grained sediment sourced from soil-mantled hillslopes and mineral-scale grussification.  
539 Conceptual models that predict continuously coarsening hillslope sediment supply with  
540 increasing catchment erosion rate may accurately reflect grain size changes in the total sediment  
541 flux (Scherler et al., 2017; Sklar et al., 2017; Shobe et al., 2018); however, bed sediment grain  
542 size responsible for setting channel geometry appears insensitive to increases in catchment  
543 erosion rate once erosion rates exceed  $E_{crit}$  and coarse sediment is supplied from bedrock cliffs  
544 and landslides. Constant bed sediment grain size across a wide range of erosion rates exceeding  
545  $E_{crit}$  in the NSJM and SGM, implies a weak feedback between time-dependent weathering  
546 processes, sediment grain size delivered to rivers, and channel morphology, and instead, bedrock  
547 fracture spacing is more strongly coupled to the grain size of bed sediment that mantles channels  
548 in steep, rapidly eroding landscapes.

549 Although weathering controls on bed sediment grain size appear minimal in steep  
550 mountain ranges where catchment erosion rates exceed  $E_{crit}$ ,  $E_{crit}$  reflects the efficiency of soil  
551 transport and soil production within a landscape, and  $E_{crit}$  varies over at least two orders of  
552 magnitude globally as a function of climate, lithology, and bedrock fracture spacing (Neely et al.,  
553 2019). Thus, changes in climate, lithology, or bedrock fracture spacing additionally affect the  
554 grain size of bed sediment in rivers by changing  $E_{crit}$ , the catchment erosion rate below which  
555 sediment grain size fines as a function of residence time on gentle, soil-mantled hillslopes.  
556 Where soil production and transport are efficient, landscapes retain gentle, continuously soil-  
557 mantled hillslopes at more rapid channel incision rates, and bed sediment grain size can still be  
558 controlled by hillslope weathering rather than bedrock fracture spacing. Through these  
559 feedbacks, changes in climate and rock properties are coupled to changes in channel incision by  
560 affecting  $E_{crit}$  and the grain size of sediment delivered to river channels, in addition to affecting  
561 stream discharge or the strength of bedrock in river channels (Murphy et al., 2016).

562 At the watershed scale, changes in sediment grain size observed within and between the  
563 NSJM and SGM have implications for interpreting channel morphodynamics in headwater and  
564 fluvial channels. Within the NSJM and SGM, downstream coarsening trends are consistent with  
565 downstream increases in unit stream power along steep, constant-gradient headwater channels  
566 (e.g. Brummer and Montgomery, 2003); however, comparing between the NSJM and SGM,  
567 headwater channels show similar channel gradients of 33-35°, despite ~5× coarser sediment  
568 grain size in the NSJM than the SGM (DiBiase et al., 2018). Steep, headwater channel  
569 morphodynamics appear relatively insensitive sediment grain size contrasts between these two  
570 landscapes, which is consistent with an interpretation that mass-wasting processes dominate  
571 sediment transport across channel reaches with gradients that approach frictional stability limits

572 for loose sediment (Prancevic et al., 2014). In contrast, fluvial channel gradients are steeper in  
573 the NSJM than the SGM, reflecting grain size differences between these landscapes and  
574 confirming prior interpretations of controls on fluvial channel steepness in these landscapes  
575 (DiBiase et al., 2018). Yet, it remains less clear how observed downstream patterns in grain size  
576 impact the drainage density and concavity of colluvial and fluvial channel networks (e.g.  
577 Gasparini et al., 2004).

## 578 **6. Conclusions**

579 Our analysis from the NSJM and SGM shows that surface sediment grain size is  
580 primarily affected by three factors: (1) grain size sorting during sediment transport processes that  
581 operate on hillslopes and in colluvial and fluvial channels; (2) inherited bedrock fracture spacing,  
582 which controls the initial grain size of sediment delivered from hillslopes to channels; and (3)  
583 catchment erosion rate, which controls the abundance of bare-bedrock hillslopes and the  
584 residence time of sediment in the weathering zone. In both landscapes, bed sediment grain size  
585 coarsens downstream throughout steep, headwater colluvial channels and fines downstream  
586 throughout fluvial channels at larger drainage areas. The transition from downstream coarsening  
587 to downstream fining at fluvial channel heads is consistent with a change in dominant sediment  
588 transport process at this location, from mass-wasting in headwater channels to fluvial  
589 entrainment downstream. When accounting for landscape position, surface sediment grain size is  
590 coarser in the NSJM than in the SGM, reflecting the contrast in bedrock fracture spacing  
591 measured on cliffs. The connection between fracture spacing and grain size is strongest once  
592 bare bedrock hillslopes emerge. In contrast to prior conceptual models, once bedrock hillslopes  
593 emerge, surface sediment grain size appears to be insensitive to further increases in erosion rates  
594 and hillslope bedrock exposure.

595 Comparison between bed-sediment grain size and catchment erosion rates suggests that  
596 emergence of bedrock cliffs on steep hillslopes imparts a threshold condition for the bed-state of  
597 river channels, where coarse sediment delivered from bedrock cliffs and headwater colluvial  
598 channels accumulates in steep fluvial channels, and finer sediment is winnowed downstream.  
599 This result is supported by observed downstream fining trends in the fluvial networks of the  
600 NSJM and SGM and contradicts conceptual models that predict continuously coarsening bed  
601 sediment grain size with increasing catchment erosion rate and bare-bedrock hillslope  
602 abundance. Instead, this result implies strong feedbacks between bedrock fracturing, bed  
603 sediment grain size, and the efficiency of river incision in steep mountain ranges, whereby the  
604 transition from soil-mantled to bedrock hillslopes emerges as a key control on the sensitivity of  
605 channel-bed sediment cover to bedrock fracture density.

## 606 **Acknowledgments**

607 Project supported by National Science Foundation grant EAR-1608014 to R. DiBiase.  
608 Low-altitude aerial imagery was acquired by Pictometry Corporation. Airborne lidar-derived  
609 topographic data was acquired by National Center for Airborne Laser Mapping. 3-D point clouds  
610 and digital orthophotos are available through *OpenTopography.org* and PSU scholarsphere data  
611 repository (<https://scholarsphere.psu.edu/>). Data tables containing bedrock fracture spacing  
612 measurements and stream grain size measurements are provided as supplementary tables. We  
613 acknowledge Angeles National Forest, San Bernardino National Forest, and Mt. San Jacinto  
614 State Park for continued trail maintenance enabling access to field sites. We thank J. Carr, J. Del

615 Vecchio, E. Greenberg, and P. Silverhart for field assistance, and we thank McLanahan's  
 616 downtown market for providing a comfortable working environment during the preparation of  
 617 this manuscript.

## 618 **References**

- 619 Attal, M., & Lavé, J. (2006). Changes of bedload characteristics along the Marsyandi River  
 620 (central Nepal): Implications for understanding hillslope sediment supply, sediment load  
 621 evolution along fluvial networks, and denudation in active orogenic belts. in *Tectonics,*  
 622 *Climate, and Landscape Evolution*, Willett, S. D., Hovius, N, Brandon, M. T., & Fisher,  
 623 D. (eds). *Geological Society of America Special Paper*, 398, 143–171.  
 624 [https://doi.org/10.1130/2006.2398\(09\)](https://doi.org/10.1130/2006.2398(09)).
- 625 Attal, M., & Lavé, J. (2009). Pebble abrasion during fluvial transport: experimental results and  
 626 implications for the evolution of the sediment load along rivers. *Journal of Geophysical*  
 627 *Research*, 114, F04023. <https://doi.org/10.1029/2009JF001328>
- 628 Attal, M., S. M. Mudd, M. D. Hurst, B. Weinman, K. Yoo, & M. Naylor (2015). Impact of  
 629 change in erosion rate and landscape steepness on hillslope and fluvial sediments grain  
 630 size in the Feather River basin (Sierra Nevada, California), *Earth Surface Dynamics*, 3,  
 631 201–222. <https://doi.org/10.5194/esurf-3-201-2015>
- 632 Barton, C. A., & Zoback, M. D. (1992). Self-similar distribution and properties of macroscopic  
 633 fractures at depth in crystalline rock in the Cajon Pass Scientific Drill Hole, *Journal of*  
 634 *Geophysical Research*, 97(B4), 5181–5200, <https://doi.org/10.1029/91JB01674>.
- 635 Benda, L., & Dunne, T. (1997a). Stochastic forcing of sediment supply to channel networks from  
 636 landsliding and debris flow, *Water Resources Research*, 33(12), 2849–2863,  
 637 <https://doi.org/10.1029/97WR02388>.
- 638 Benda, L., & Dunne, T. (1997b). Stochastic forcing of sediment routing and storage in channel  
 639 networks, *Water Resources Research*, 33(12), 2865–2880, doi:10.1029/97WR02387.
- 640 Brummer, C. J., & Montgomery, D. R. (2003). Downstream coarsening in headwater channels.  
 641 *Water Resources Research*, 39(10), 1294. <https://doi.org/10.1029/2003WR001981>
- 642 Bunte, K., & Abt, S. R. (2001). Sampling surface and subsurface particle-size distributions in  
 643 wadable gravel- and cobble-bed streams for analyses in sediment transport, hydraulics,  
 644 and Streambed monitoring (General Tech. Rep. RMRS-GTR-74). Fort Collins, CO: US  
 645 Department of Agriculture, Forest Service, Rocky Mountain Research Station.
- 646 Carson, M. A., & Petley, D. J. (1970). The existence of threshold slopes in the denudation of the  
 647 landscape, *Transactions of the Institute of British Geographers*, 49, 71–95.  
 648 <https://doi.org/10.2307/621642>
- 649 Dershowitz, W. S., & Herda, H. H. (1992). Interpretation of fracture spacing and intensity, Proc.  
 650 U.S. Rock Mech. Symp. 33rd, 10.
- 651 DiBiase, R. A., Whipple, K. X., Heimsath, A. M., & Ouimet, W. B. (2010). Landscape form and  
 652 millennial erosion rates in the San Gabriel Mountains, CA, *Earth and Planetary Science*  
 653 *Letters*, 289(1–2), 134–144, <https://doi.org/10.1016/j.epsl.2009.10.036>.

- 654 DiBiase, R. A., & Whipple, K. X. (2011). The influence of erosion thresholds and runoff  
655 variability on the relationships among topography, climate, and erosion rate, *Journal of*  
656 *Geophysical Research: Earth Surface*, 116, F04036,  
657 <https://doi.org/10.1029/2011JF002095>.
- 658 DiBiase, R.A., Heimsath, A.M., & Whipple, K.X. (2012). Hillslope response to tectonic forcing  
659 in threshold landscapes. *Earth Surface Processes and Landforms*, 37(8), 855–865.  
660 <https://doi.org/10.1002/esp.3205>
- 661 DiBiase, R.A., Lamb, M.P., Ganti, V. & Booth, A.M. (2017). Slope, grain size, and roughness  
662 controls on dry sediment transport and storage on steep hillslopes. *Journal of*  
663 *Geophysical Research: Earth Surface*, 122(4), 941–960.  
664 <https://doi.org/10.1002/2016JF003970>
- 665 DiBiase, R.A., Rossi, M.W. & Neely, A.B. (2018). Fracture density and grain size controls on  
666 the relief structure of bedrock landscapes. *Geology*, 46(5), 399–402.  
667 <https://doi.org/10.1130/G40006.1>
- 668 Duller, R.A., Whittaker, A.C., Fedele, J.J., Whitchurch, A.L., Springett, J., Smithells, R.,  
669 Fordyce, S. & Allen, P.A. (2010). From grain size to tectonics. *Journal of Geophysical*  
670 *Research: Earth Surface*, 115(F3). <https://doi.org/10.1029/2009JF001495>
- 671 Fletcher, R.C., & Brantley, S.L. (2010). Reduction of bedrock blocks as corestones in the  
672 weathering profile: observations and model. *American Journal of Science*, 310(3), 131–  
673 164. <https://doi.org/10.2475/03.2010.01>
- 674 Gasparini, N. M., Tucker, G. E., & Bras, R. L. (2004). Network-scale dynamics of grain-size  
675 sorting: Implications for downstream fining, stream-profile concavity, and drainage basin  
676 morphology. *Earth Surface Processes and Landforms*, 29(4), 401–421.  
677 <https://doi.org/10.1002/esp.1031>
- 678 Glade, R.C., Anderson, R.S., & Tucker, G.E. (2017). Block-controlled hillslope form and  
679 persistence of topography in rocky landscapes. *Geology*, 45(4), 311–314.  
680 <https://doi.org/10.1130/G38665.1>
- 681 Hack, J. T. (1957). Studies of longitudinal stream profiles in Virginia and Maryland, U.S. Geol.  
682 Surv. Prof. Pap., 294-B, 97.
- 683 Heimsath, A. M., DiBiase, R. A., & Whipple, K. X. (2012). Soil production limits and the  
684 transition to bedrock-dominated landscapes, *Nature Geoscience*, 5, 210–214,  
685 <https://doi.org/10.1038/NGEO1380>.
- 686 Hooker, J. N., Laubach, S. E., & Marrett, R. (2014). A universal power-law scaling exponent for  
687 fracture apertures in sandstones, *GSA Bulletin*, 126(9-10), 1340–1362,  
688 <https://doi.org/10.1130/B30945.1>.
- 689 Jennings, C.W., Strand, R.G., & Rogers, T.H. (1977). Geologic map of California: California  
690 Division of Mines and Geology, scale 1:750,000
- 691 Kirby E., & Whipple K. X. (2012). Expression of active tectonics in erosional landscapes.  
692 *Journal of Structural Geology*, 44, 54–75. <https://doi.org/10.1016/j.jsg.2012.07.009>
- 693 Kirkby, M.J. & Statham, I. (1975). Surface stone movement and scree formation. *The Journal of*  
694 *Geology*, 83(3), 349–362. <https://doi.org/10.2307/30059027>

- 695 Lague, D., Hovius, N. & Davy, P. (2005). Discharge, discharge variability, and the bedrock  
696 channel profile. *Journal of Geophysical Research: Earth Surface*, 110, F4,  
697 <https://doi.org/10.1029/2004JF000259>
- 698 Lamb, M. P., Dietrich, W. E., & Venditti, J. G. (2008). Is the critical Shields stress for incipient  
699 sediment motion dependent on channel-bed slope? *Journal of Geophysical Research:*  
700 *Earth Surface*, 113, F02008, <https://doi.org/10.1029/2007JF000831>
- 701 Lamb, M. P., Scheingross, J. S., Amidon, W. H., Swanson, E., & Limaye, A. (2011). A model  
702 for fire-induced sediment yield by dry ravel in steep landscapes, *Journal of Geophysical*  
703 *Research: Earth Surface*, 116, F03006, <https://doi.org/10.1029/2010JF001878>
- 704 Lamb, M. P., Brun, F. & Fuller, B.M. (2017). Direct measurements of lift and drag on shallowly  
705 submerged cobbles in steep streams: Implications for flow resistance and sediment  
706 transport. *Water Resources Research*, 53(9), 7607–7629.  
707 <https://doi.org/10.1002/2017WR020883>
- 708 Menting, F., Langston, A. L., & Temme, A. J. A. M. (2015). Downstream fining, selective  
709 transport, and hillslope influence on channel bed sediment in mountain streams, Colorado  
710 Front Range, USA. *Geomorphology*, 239, 91–105.  
711 <https://doi.org/10.1016/j.geomorph.2015.03.018>
- 712 Messenzehl, K., Viles, H., Otto, J.-C., Ewald, A., & Dikau, R. (2018). Linking rock weathering,  
713 rockwall instability and rockfall supply on talus slopes in glaciated hanging valleys  
714 (Swiss Alps). *Permafrost and Periglacial Processes*, 29, 135–151.  
715 <https://doi.org/10.1002/ppp.1976>
- 716 Milodowski, D. T., Mudd, S. M., & Mitchard, E. T. A. (2015). Topographic roughness as a  
717 signature of the emergence of bedrock in eroding landscapes, *Earth Surface Dynamics*,  
718 3(4), 483–499, <https://doi.org/10.5194/esurf-3-483-2015>
- 719 Molnar, P., Anderson, R. S., & Anderson, S. P. (2007). Tectonics, fracturing of rock, and  
720 erosion, *Journal of Geophysical Research: Earth Surface*, 112, F03014,  
721 <https://doi.org/10.1029/2005JF000433>
- 722 Montgomery, D. R., & Foufoula-Georgiou, E. (1993). Channel network representation using  
723 digital elevation models, *Water Resources Research*, 29, 1178–1191.  
724 <https://doi.org/10.1029/93WR02463>
- 725 Moore, J. R., Sanders, J. W., Dietrich, W. E., & Glaser, S. D. (2009). Influence of rock mass  
726 strength on the erosion rate of alpine cliffs, *Earth Surface Processes and Landforms*, 34,  
727 1339–1352, <https://doi.org/10.1002/esp.1821>
- 728 Murphy, B. P., Johnson, J. P. L., Gasparini, N. M., & Sklar, L. S. (2016). Chemical weathering  
729 as a mechanism for the climatic control of bedrock river incision. *Nature*, 532(7598),  
730 223–227. <https://doi.org/10.1038/nature17449>
- 731 Neely, A. B., DiBiase, R. A., Corbett, L. B., Bierman, P. R., & Caffee, M.W. (2019). Bedrock  
732 fracture density controls on hillslope erodibility in steep, rocky landscapes with patchy  
733 soil cover, southern California, USA. *Earth and Planetary Science Letters*, 522, 186–197.  
734 <https://doi.org/10.1016/j.epsl.2019.06.011>

- 735 Palmstrom, A. (2005). Measurements of and correlations between block size and rock quality  
736 designation (RQD). *Tunnelling and Underground Space Technology*, 20(4), 362–377.  
737 <https://doi.org/10.1016/j.tust.2005.01.005>
- 738 Parker, G. (1990). Surface-based transport relation for gravel rivers, *Journal of Hydraulic*  
739 *Research*, 20, 417–436. <https://doi.org/10.1080/00221689009499058>
- 740 Pfeiffer, A. M., Finnegan, N. J., & Willenbring, J. K. (2017). Sediment supply controls  
741 equilibrium channel geometry in gravel rivers, *Proceedings of the National Academy of*  
742 *Sciences*, 114(13), 3346–3351, <https://doi.org/10.1073/pnas.1612907114>
- 743 Phillips, C. B., & Jerolmack, D. J. (2016). Self-organization of river channels as a critical filter  
744 on climate signals, *Science*, 352(6286), 694–697, <https://doi.org/10.1126/science.aad3348>
- 745 Pizzuto, J.E. (1995). Downstream fining in a network of gravel-bedded rivers. *Water Resources*  
746 *Research*, 31(3), 753–759. <https://doi.org/10.1029/94WR02532>
- 747 Portenga, E. W., & Bierman, P. R. (2011). Understanding Earth's eroding surface with <sup>10</sup>Be.  
748 *GSA today*, 21(8), 4–10. <http://dx.doi.org/10.1130/G1111A.1>
- 749 Prancevic, J. P., Lamb, M. P., & Fuller, B. M. (2014). Incipient sediment motion across the river  
750 to debris-flow transition. *Geology*, 42(3), 191–194. <https://doi.org/10.1130/G34927.1>
- 751 Rapp, A. (1960). Recent development of mountain slopes in Karkevagge and surroundings,  
752 northern Scandinavia, *Geografiska Annaler*, 42, 65–200, <https://doi.org/10.2307/520126>
- 753 Rickenmann, D. (2001). Comparison of bed load transport in torrents and gravel bed streams.  
754 *Water Resources Research*, 37(12), 3295–3305. <https://doi.org/10.1029/2001WR000319>
- 755 Riebe, C. S., Hahm, W. J., & Brantley, S. L. (2017). Controls on deep critical zone architecture:  
756 A historical review and four testable hypotheses. *Earth Surface Processes and*  
757 *Landforms*, 42(1), 128–156. <https://doi.org/10.1002/esp.4052>
- 758 Roda-Boluda, D. C., D'Arcy, M., McDonald, J., & Whittaker, A. C. (2018). Lithological controls  
759 on hillslope sediment supply: Insights from landslide activity and grain size distributions.  
760 *Earth Surface Processes and Landforms*, 43(5), 956–977.  
761 <https://doi.org/10.1002/esp.4281>
- 762 Rossi, M. W. (2014), Hydroclimatic Controls on Erosional Efficiency in Mountain Landscapes  
763 [Ph.D. Thesis]: Tempe, Arizona, Arizona State University.
- 764 Scherler, D., DiBiase, R. A., Fisher, G. B., & Avouac, J.-P. (2017). Testing monsoonal controls  
765 on bedrock river incision in the Himalaya and Eastern Tibet with a stochastic-threshold  
766 stream power model. *Journal of Geophysical Research: Earth Surface*, 122, 1389–1429.  
767 <https://doi.org/10.1002/2016JF004011>
- 768 Shobe, C. M., Tucker, G. E., & Anderson, R. S. (2016). Hillslope-derived blocks retard river  
769 incision. *Geophysical Research Letters*, 43, 5070–5078.  
770 <https://doi.org/10.1002/2016GL069262>
- 771 Shobe, C. M., Tucker, G. E. & Rossi, M. W. (2018). Variable-threshold behavior in rivers arising  
772 from hillslope-derived blocks. *Journal of Geophysical Research: Earth Surface*, 123(8),  
773 1931–1957. <https://doi.org/10.1029/2017JF004575>

- 774 Sklar, L. S., & Dietrich, W. E. (2004). A mechanistic model for river incision into bedrock by  
775 saltating bed load. *Water Resources Research*, 40, W06301.  
776 <https://doi.org/10.1029/2003WR002496>
- 777 Sklar, L. S., & Dietrich, W. E. (2006). The role of sediment in controlling steady-state bedrock  
778 channel slope: Implications of the saltation-abrasion model. *Geomorphology*, 82(1–2),  
779 58–83. <https://doi.org/10.1016/j.geomorph.2005.08.019>
- 780 Sklar, L. S., Riebe, C. S., Marshall, J. A., Genetti, J., Leclere, S., Lukens, C. L., & Merces, V.  
781 (2017). The problem of predicting the size distribution of sediment supplied by hillslopes  
782 to rivers. *Geomorphology*, 277, 31–49. <https://doi.org/10.1016/j.geomorph.2016.05.005>
- 783 Stock, J. D., & Dietrich, W. E. (2006), Erosion of steepland valleys by debris flows, *GSA*  
784 *Bulletin*, 118, 1125–1148, <https://doi.org/10.1130/B25902.1>
- 785 Wolman, M. G. (1954). A method of sampling coarse river-bed material. *Eos, Transactions of*  
786 *the American Geophysical Union*, 35(6), 951–956.  
787 <https://doi.org/10.1029/TR035i006p00951>
- 788 Yager, E.M., Kirchner, J. W., & Dietrich, W. E. (2007). Calculating bed load transport in steep  
789 boulder bed channels. *Water Resources Research*, 43(7).  
790 <https://doi.org/10.1029/2006WR005432>
- 791 Zimmermann, A., Church, M. & Hassan, M. A. (2010). Step-pool stability: Testing the jammed  
792 state hypothesis. *Journal of Geophysical Research: Earth Surface*, 115(F2).  
793 <https://doi.org/10.1029/2009JF001365>  
794  
795

796 **Table 1.** Surface sediment grain size and catchment attributes at fluvial channel head and fan  
 797 <sup>10</sup>Be sample locations

798

<sup>1</sup> Fans	Drainage area (km <sup>2</sup> )	Outlet Latitude (°)	Outlet Longitude (°)	Erosion rate, <i>E</i> (m kyr <sup>-1</sup> )	<sup>2</sup> <i>f</i> <sub>bedrock</sub>	D <sub>50</sub> (cm)	Number of Grains Measured	D <sub>50</sub> Fracture (cm)	Bedrock Fracture Area Surveyed (m <sup>2</sup> )
SG1602	28	34.1621	-117.6376	1.28 ± 0.19	0.33*	9±1	105	75	9,325
SG07-06*	13	34.2046	-118.0924	0.57 ± 0.11	0.14	22±4	674	x	0
SG08-09*	18	34.3692	-117.8394	0.37 ± 0.04	0.06	8±0.7	586	x	0
SJ0806	28	33.8738	-116.6796	0.151 ± 0.012	0.21*	45±4	635	325	25,887
SJ0807	11	33.8751	-116.6732	0.086 ± 0.008	0.27*	60±13	175	304	46,938
SJ1703	9.8	33.8397	-116.6137	0.53 ± 0.07	0.58*	29±8	119	239	2,388
Headwater catchments	Drainage area (km <sup>2</sup> )	Outlet Latitude (°)	Outlet Longitude (°)	Erosion rate, <i>E</i> (m kyr <sup>-1</sup> )	<sup>2</sup> <i>f</i> <sub>bedrock</sub>	D <sub>50</sub> channel (cm)	Number of Grains Measured	D <sub>50</sub> Fracture (cm)	Bedrock Fracture Area Surveyed (m <sup>2</sup> )
SG127	2.5	34.2187	-118.0855	0.68 ± 0.08	0.25	39±13	125	x	0
SG128	2.1	34.3381	-118.0106	0.036 ± 0.004	0.04	3±1	114	66	90
SG131	2.2	34.3659	-117.9931	0.085 ± 0.013	0.01	0.8±0.2	102	46	78
SG132	2.2	34.3652	-117.99	0.093 ± 0.009	0.01	3±1	108	x	0
SG1601	1.2	34.1906	-117.6434	0.96 ± 0.16	0.23	30±4	377	x	0
SG1605	1.2	34.2036	-117.5867	2.2 ± 0.4	0.60	27±4	271	51	3,333
SG1608	4.3	34.214	-117.6075	0.63 ± 0.09	0.25*	23±2.3	559	69	4,592
SG1609	0.8	34.2226	-117.6076	0.60 ± 0.07	0.43	29±4	373	62	1,055
SG1703	1.3	34.2038	-117.6311	0.234 ± 0.024	0.25	27±2	1346	87	1,043
SG1705	1.9	34.2142	-117.6206	0.39 ± 0.05	0.41	33±1	2504	86	1,839
SG1706	1.2	34.2159	-117.5721	1.39 ± 0.19	0.68	29±3	541	89	567
SGB07	3.1	34.2979	-118.1487	0.22 ± 0.04	0.12	4±1	108	x	0
SJ0801	6.5	33.8117	-116.6428	0.040 ± 0.003	0.13±0.08**	0.5±0.1	161	x	0
SJ0804	5.4	33.7797	-116.646	0.044 ± 0.004	0.13	6±2	107	93	238
SJ0805	6.8	33.7765	-116.6485	0.061 ± 0.005	0.50	2.0±0.6	107	x	0
SJ1601	3.6	33.8329	-116.6589	0.154 ± 0.014	0.48	89±11	423	304	46,938
SJ1603	1.2	33.8296	-116.6784	0.202 ± 0.019	0.61	150±25	249	325	25,887
SJ1604	1.3	33.8357	-116.6997	0.16 ± 0.014	0.53	117±30	126	x	0
SJ1605	2.5	33.835	-116.7005	0.251 ± 0.023	0.28	114±13	461	x	0
SJ1701	0.7	33.8365	-116.6357	0.234 ± 0.023	0.41	86±5	1347	239	2,388
SJ1702	1.2	33.8298	-116.6354	0.61 ± 0.09	0.52	126±10	825	x	0

799 <sup>1</sup> All samples recorded in Neely et al., 2019 with exception of samples denoted by \*, where erosion rates are calculated from <sup>10</sup>Be concentrations  
 800 reported in DiBiase et al. (2010) and Heimsath et al. (2012) as recalculated by Neely et al. (2019). Lat, Long, and drainage area refer to  
 801 downstream-most location of grain size surveys associated with each <sup>10</sup>Be-derived erosion rate.

802 <sup>2</sup> The fraction of bare bedrock exposed on hillslopes, *f*<sub>bedrock</sub>, are reported in Neely et al., 2019 with exception of samples denoted by \*, where  
 803 *f*<sub>bedrock</sub> is estimated from linear regression between mean hillslope angle and *f*<sub>bedrock</sub> (Neely et al., 2019), and \*\*, where *f*<sub>bedrock</sub> is determined from  
 804 mapping with 0.5-m resolution imagery from ArcGIS 10.2 world-imagery (DigitalGlobe, 2014, 2017).  
 805  
 806

807 **Table 2.** Parameters used for sediment grain size fining model (Eq. 1; Fig.10)

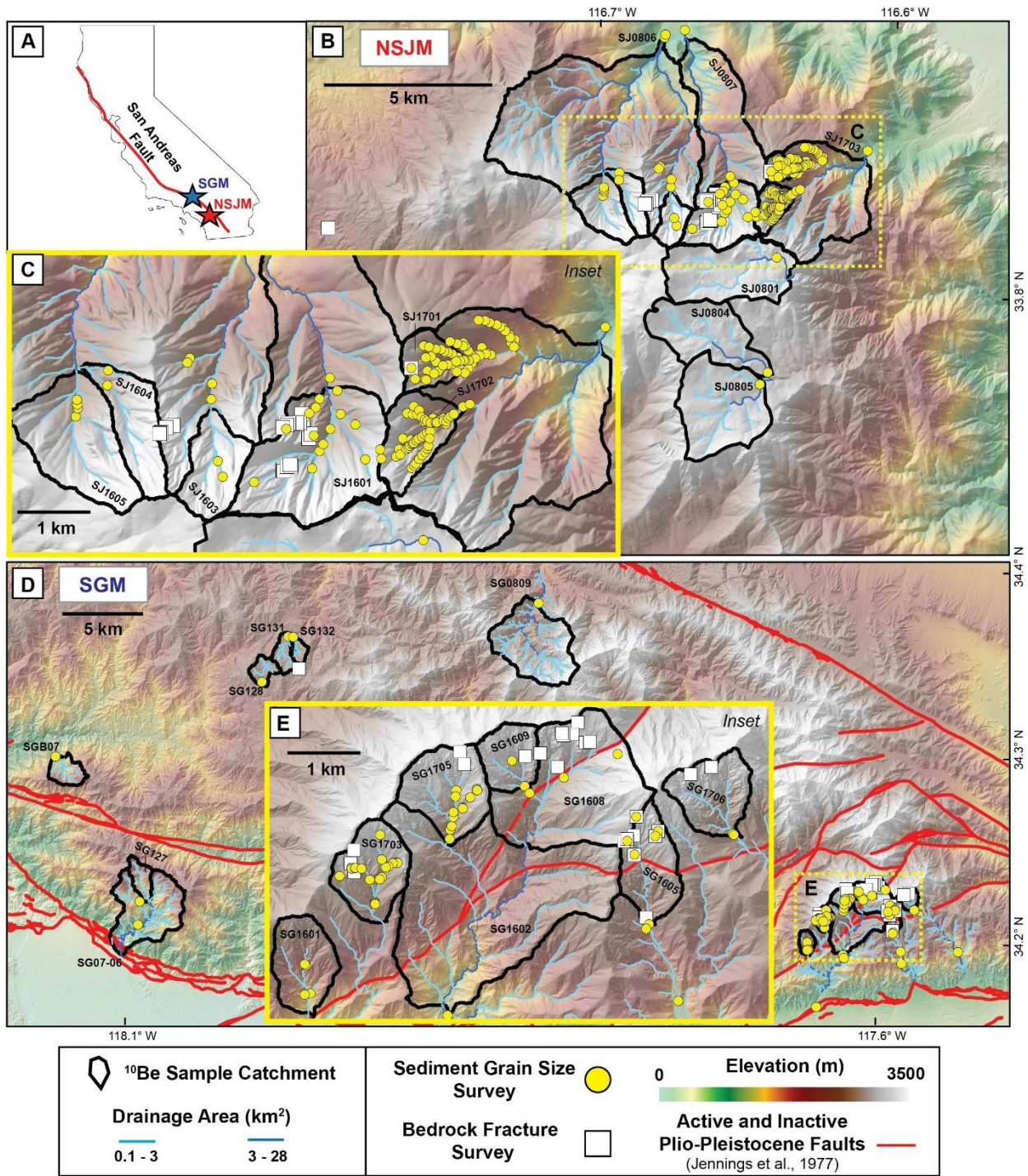
808

Model Parameters	h (m)	$\alpha$	$k_1$	$k_2$ (m kyr <sup>-1</sup> )	$k_3$	$E_{crit}$ (m kyr <sup>-1</sup> )	$D_{50 \text{ fracture}}$ (cm)	$D_{50 \text{ min}}$ (cm)
<b>NSJM</b>	1	2.27	0.4	0.05	0.4	0.08	299	0.01
<b>SGM</b>	1	0.51	0.5	0.025	0.5	0.2	63	0.01

809

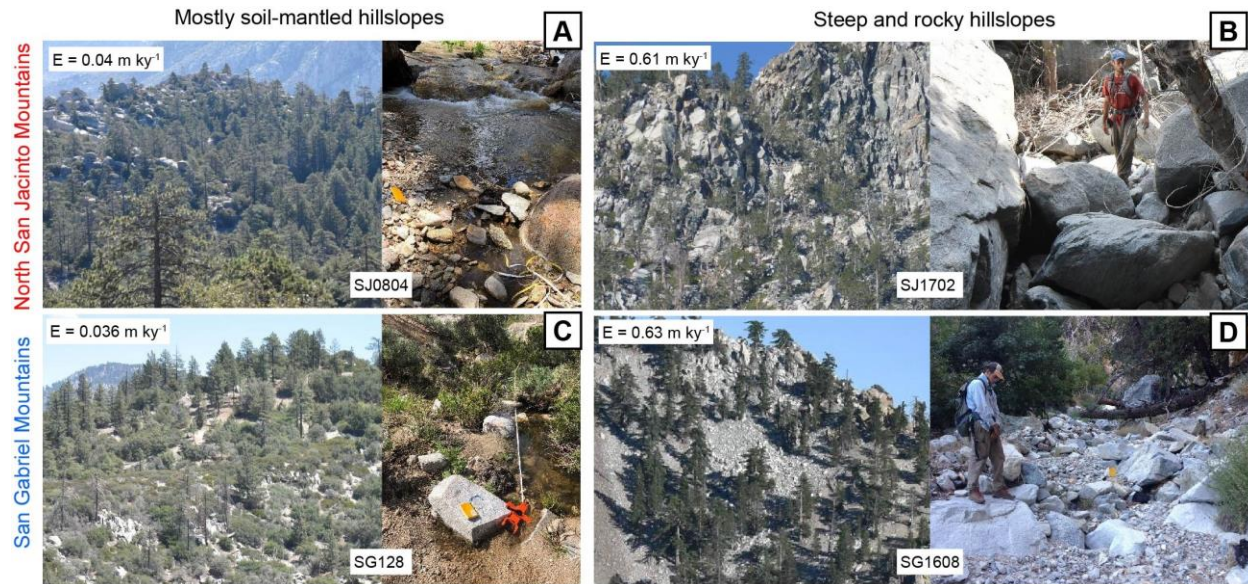
810

811



812

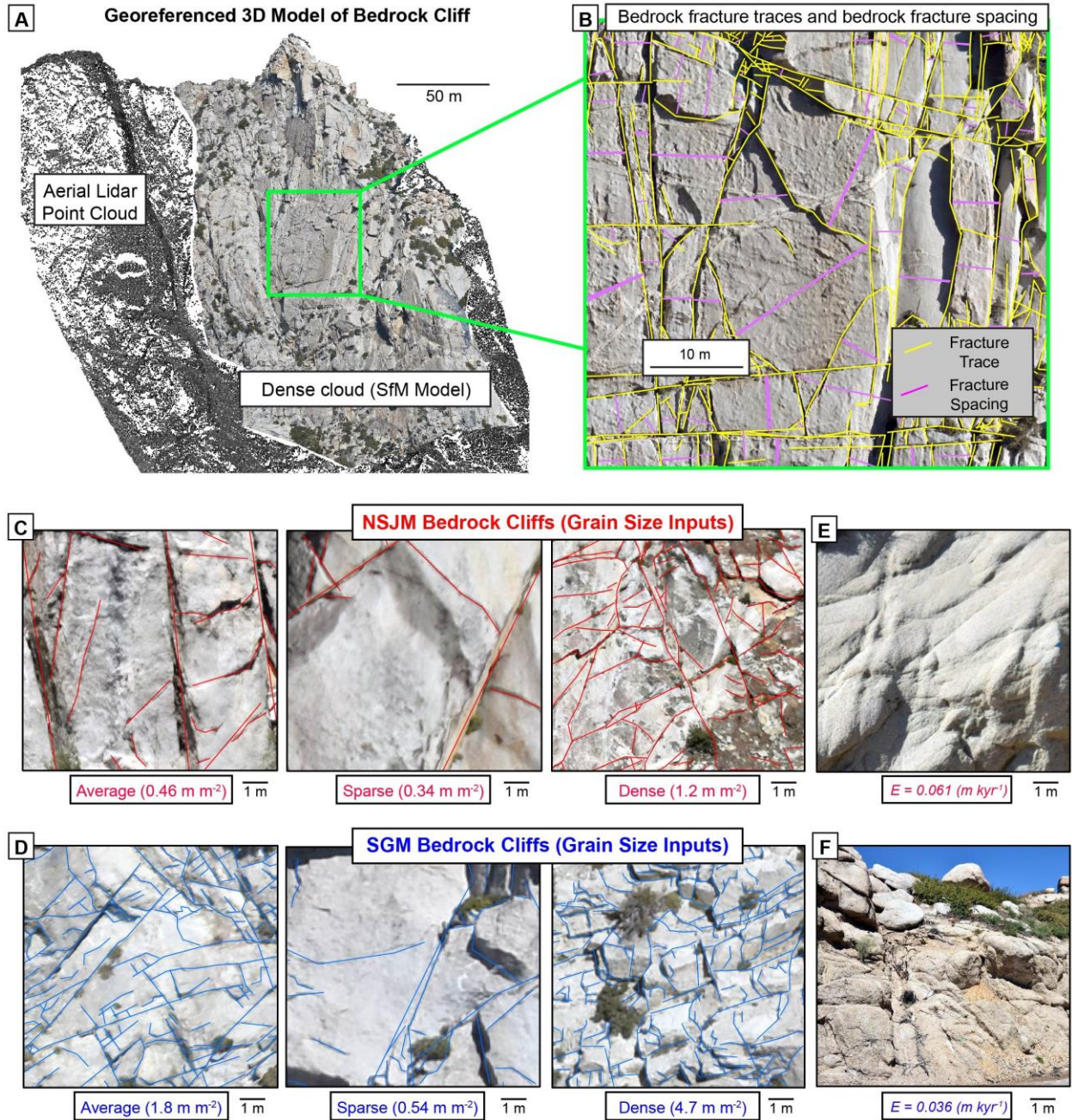
813 **Figure 1.** (A) Location of northern San Jacinto Mountains (NSJM) and San Gabriel Mountains  
 814 (SGM) in southern California, USA. (B-E) Location of sediment grain size and bedrock fracture  
 815 spacing surveys within  $^{10}\text{Be}$  sample catchments in NSJM (B-C) and SGM (D-E). Inset maps  
 816 show catchments with high-data density in (C) NSJM and (E) eastern SGM.  
 817



818

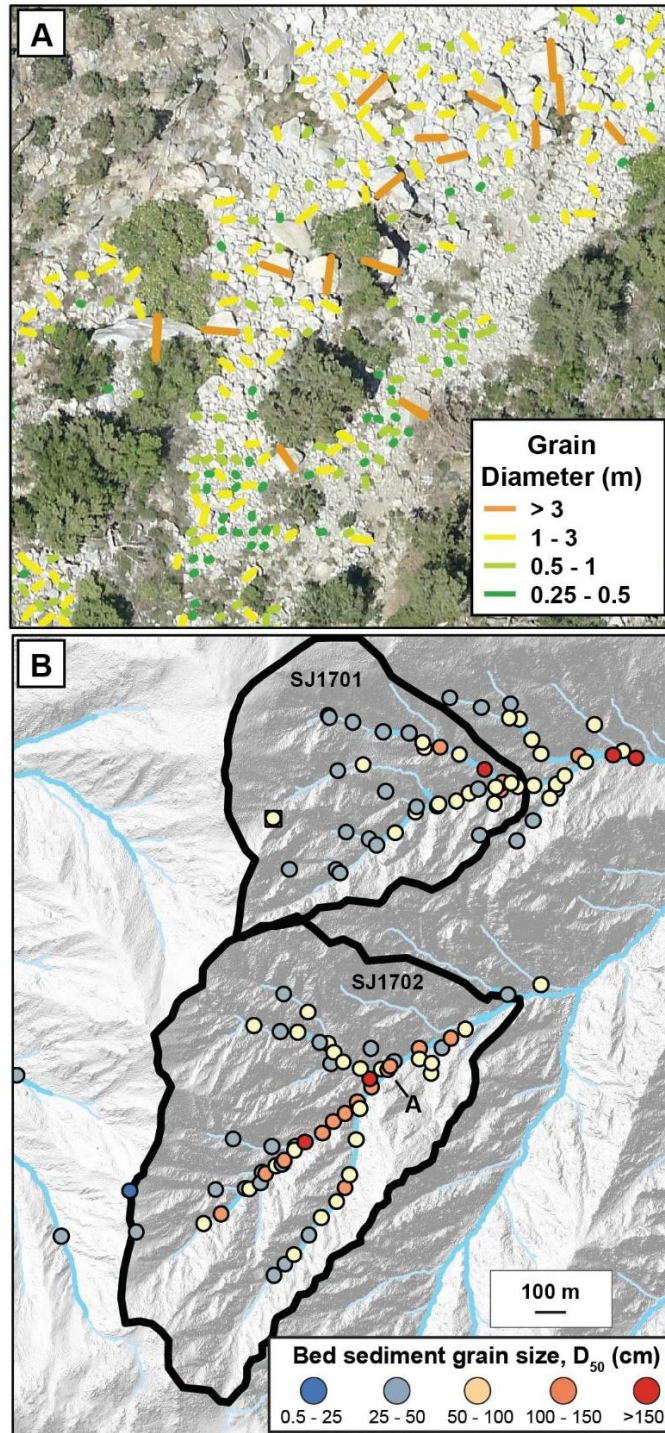
819 **Figure 2.** Example hillslopes and channel bed material from the northern San Jacinto Mountains  
820 (A, B) and San Gabriel Mountains (C, D) in soil mantled catchments (A, C) and steep  
821 catchments with bedrock cliffs (B, D). E indicates erosion rate determined from in situ  $^{10}\text{Be}$   
822 concentrations in stream sediment (DiBiase et al., 2010; Rossi, 2014; Neely et al., 2019). Scale is  
823 approximately the same for hillslope photographs and for channel bed photographs.  
824

825



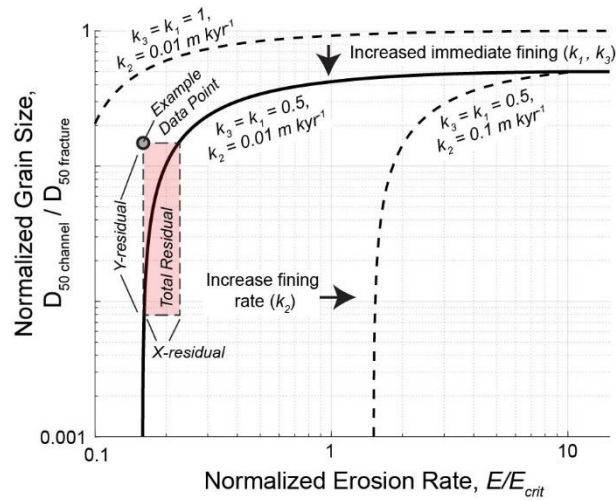
826

827 **Figure 3.** (A) Cliff SJ1603-2 shown with structure-from-motion photogrammetry (SfM) point  
 828 cloud (colorized points) aligned to the airborne lidar point cloud (black points). (B) 1-cm  
 829 resolution orthophoto extracted from region within yellow box. Yellow lines are bedrock fracture  
 830 traces used to calculate fracture density. Pink lines show bedrock fracture spacing between  
 831 fracture traces. (C-D) Orthophotos showing fracture traces and the range of bedrock fracture  
 832 densities for cliffs from the northern San Jacinto Mountains (NSJM) (C) and San Gabriel  
 833 Mountains (SGM) (D). (E-F) Field photographs show weathered bedrock in road cuts from soil-  
 834 mantled catchments in the (E) NSJM and (F) SGM.  
 835



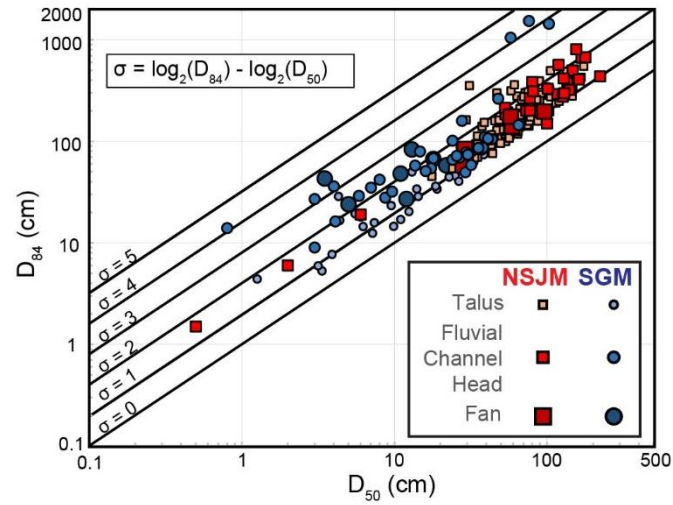
836

837 **Figure 4.** (A) Example orthophoto shows individual grain diameter measurements from Chino  
 838 Canyon in NSJM (catchment SJ1702, location shown in panel B). (B) Continuous grain diameter  
 839 measurements made throughout catchments SJ1701 and SJ1702 in NSJM are discretized into  
 840 individual grain size surveys (colored circles). Blue lines denote channel network with drainage  
 841 area >0.01 km<sup>2</sup> and black polygons outline watersheds upstream from <sup>10</sup>Be sample locations.  
 842



843

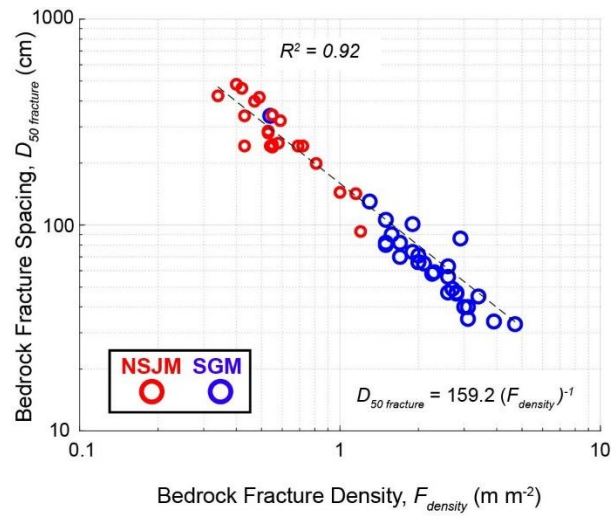
844 **Figure 5:** Predicted relationship between normalized grain size and normalized erosion rate from  
 845 hillslope sediment fining model (Eq. 1). Dashed curves illustrate model sensitivity to parameters  
 846  $k_1$ ,  $k_2$ , and  $k_3$ , assuming similar initial fining for soil-mantled and bedrock hillslopes ( $k_1 = k_3$ ).  
 847 Example data point (grey) shows example calculation of model residuals (red box). The  
 848 minimum dimension of the residual rectangle for each field-data point was used to calculate  
 849 sum-squared residuals and fit  $k_1$ ,  $k_3$ , and  $k_2$  values to field data.



850

851 **Figure 6:** Plot of  $D_{84}$  versus  $D_{50}$  for all sediment grain size distributions highlighting similar  
852 range of sorting coefficient,  $\sigma$ , for all sample types and for both landscapes.  
853

854



855

856 **Figure 7.** Bedrock fracture density,  $F_{\text{density}}$ , plotted against median bedrock fracture spacing,  $D_{50}$   
857 *fracture*, measured for each cliff in the northern San Jacinto Mountains (NSJM; N = 21) and San  
858 Gabriel Mountains (SGM; N = 29).

859

860

861

862

863

864

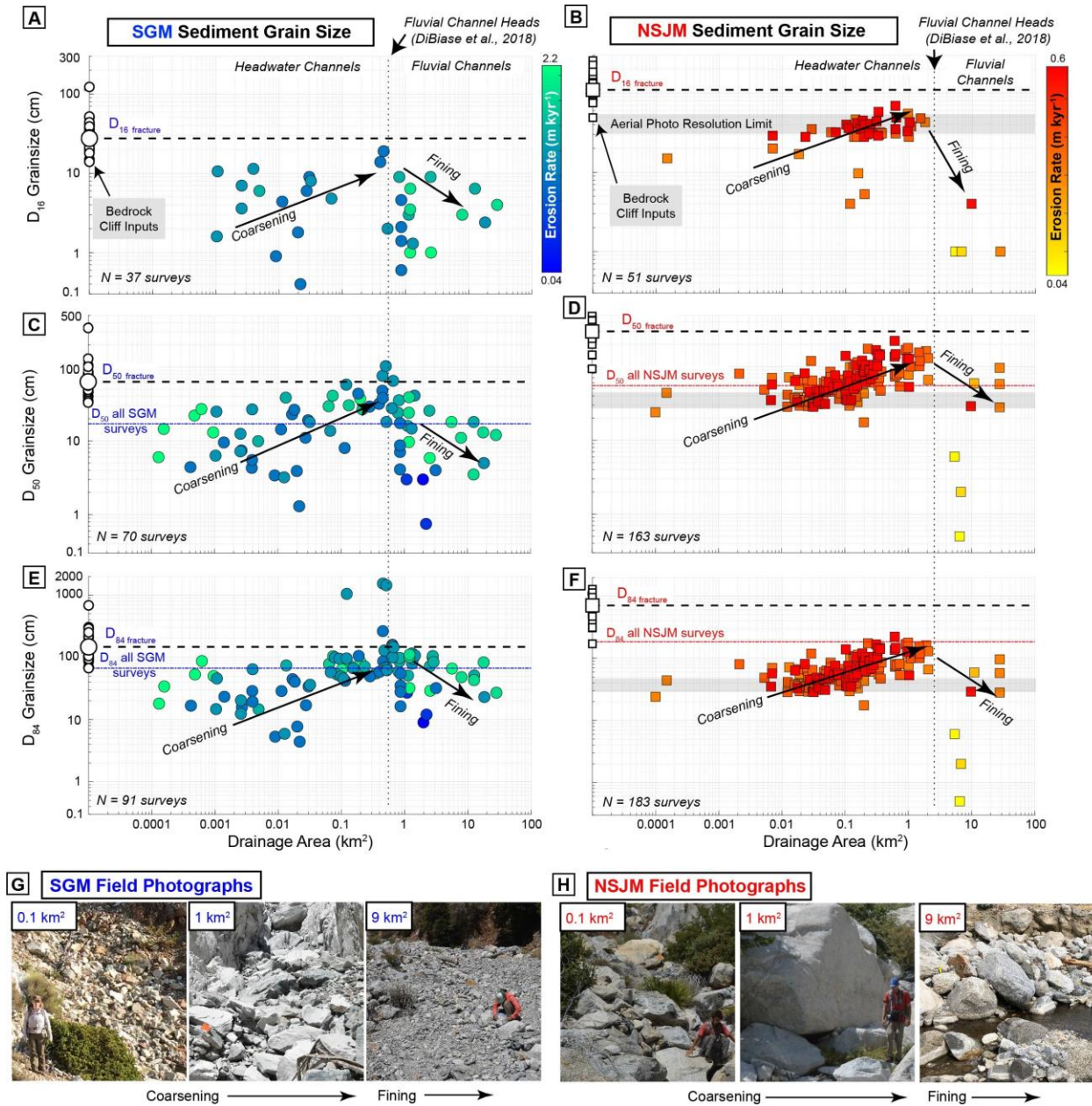
865

866

867

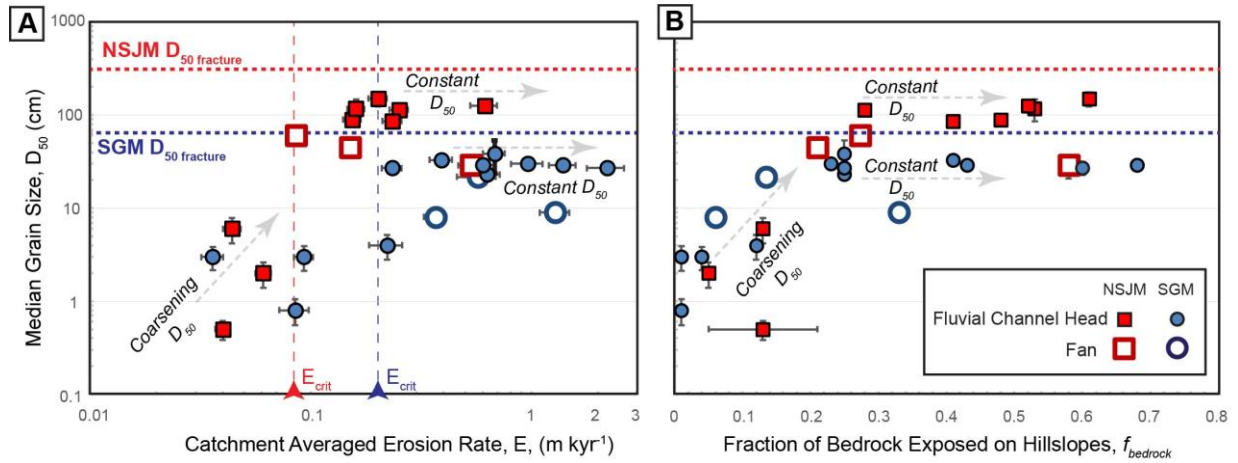
868

869



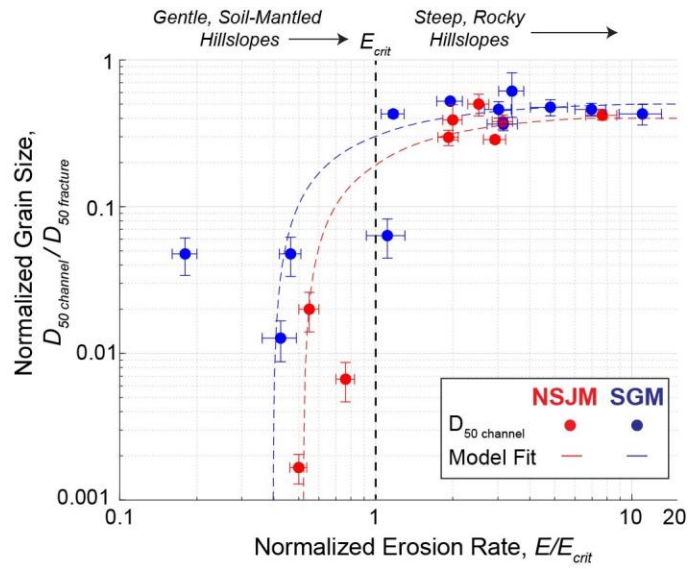
870

871 **Figure 8.** Downstream trends in sediment grain size for the San Gabriel Mountains (SGM, left  
 872 panels) and northern San Jacinto Mountains (NSJM, right panels). (A-B) Downstream trends in  
 873  $D_{16}$  (A-B),  $D_{50}$  (C-D), and  $D_{84}$  (E-F); fracture spacing measured on bedrock cliffs is marked on  
 874 the y-axis with white symbols, with large white symbol and black dashed line representing the  
 875  $D_{16}$  (A-B),  $D_{50}$  (C-D), and  $D_{84}$  (E-F) of summed fracture spacing distribution from all cliffs in  
 876 each landscape. The  $D_{50}$  and  $D_{84}$  from all channel surveys is marked in both landscapes with a  
 877 colored horizontal line. Symbol colors correspond to catchment averaged erosion rate associated  
 878 with each grain size survey. Aerial photograph resolution limit (28–48 cm) is marked on NSJM  
 879 plots. The number of surveys with resolvable  $D_{16}$ ,  $D_{50}$ , or  $D_{84}$  is marked in bottom left corner of  
 880 each panel. (G-H) Field photographs of sediment grain size at increasing drainage areas. All  
 881 photographs have approximately the same scale.  
 882



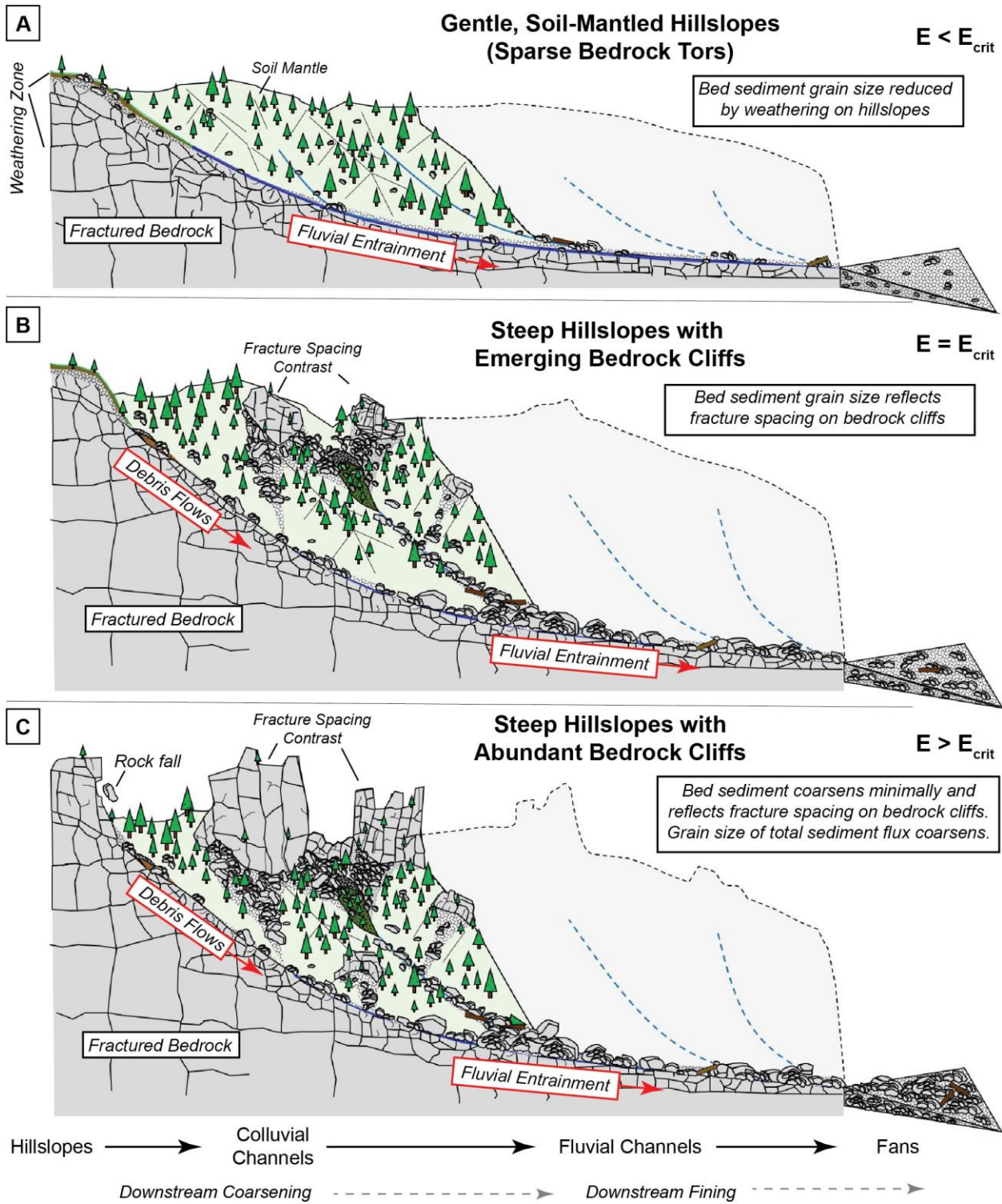
883

884 **Figure 9:** Trends in median grainsize,  $D_{50}$ , as a function of (A) increasing catchment erosion rate  
 885 and (B) bare-bedrock hillslope abundance in the northern San Jacinto Mountains (NSJM, red)  
 886 and San Gabriel Mountains (SGM, blue). Colored arrows and vertical dashed lines show  
 887 catchment erosion rate  $E_{crit}$ , above which bedrock hillslope abundance increases systematically  
 888 (Neely et al., 2019). Fluvial channel head data points reflect sample catchments with drainage  
 889 areas ranging from 0.5–7  $km^2$  in the NSJM and 0.05–3  $km^2$  in the SGM. Fan data points indicate  
 890 measurements from mountain-front catchment outlets with drainage areas larger than 7  $km^2$ .  
 891



892

893 **Figure 10.** Plots show comparison between modeled sediment grain size delivered from  
 894 hillslopes and measured sediment grain size at fluvial channel heads. Parameters used for model  
 895 are listed in table 2.  $E_{crit}$  is erosion rate above which bedrock exposure on hillslopes  
 896 systematically increases.



897  
898  
899

**Figure 11.** Conceptual model showing landscape-scale grain size patterns as a function of increasing catchment erosion rate,  $E$ , and bare-bedrock hillslope abundance,  $f_{bedrock}$ .